

1 Methane optical density measurements with an integrated path 2 differential absorption lidar from an airborne platform

3
4 **Haris Riris,^{a*} Kenji Numata,^a Stewart Wu,^a Brayler Gonzalez,^a Michael Rodriguez,^b Stan
5 Scott,^a Stephan Kawa,^a Jianping Mao^c**

6 ^aNASA Goddard Space Flight Center, 8800 Greenbelt Rd., Greenbelt, MD 20771,

7 ^bSigma Space Corporation., 4600 Forbes Blvd., Lahnam, MD 20706,

8 ^cEarth System Science Interdisciplinary Center (ESSIC), University of Maryland, College Park, MD 20740

9

10 **Abstract.** We report on an airborne demonstration of atmospheric methane (CH₄) measurements with an Integrated
11 Path Differential Absorption (IPDA) lidar using an optical parametric amplifier (OPA) and optical parametric
12 oscillator (OPO) laser transmitter and sensitive avalanche photodiode detector. The lidar measures the atmospheric
13 CH₄ absorption at multiple, discrete wavelengths near 1650.96 nm. The instrument was deployed in the fall of 2015,
14 aboard NASA's DC-8 airborne laboratory along with an in-situ spectrometer and measured CH₄ over a wide range
15 of surfaces and atmospheric conditions from altitudes of 2 km to 13 km. In this paper, we will show the results from
16 our flights, compare the performance of the two laser transmitters, and identify areas of improvement for the lidar.

17

18 **Keywords:** lidar, spectroscopy, methane, optical parametric amplifiers, optical parametric oscillators, airborne
19 instruments.

20

21 *E-mail: haris.riris@nasa.gov

22

23 1 Introduction

24 Methane (CH₄) is the second most important anthropogenic greenhouse gas (GHG) with a higher
25 radiative forcing potential than Carbon Dioxide (CO₂) on a per molecule basis¹, making
26 anthropogenic CH₄ a critical target for mitigation. The current CH₄ global mixing ratio is 1852
27 parts per billion (ppb)^{2, 3}. Anthropogenic CH₄ is responsible for a significant portion of the
28 global warming produced by all well-mixed greenhouse gases and contributes to the formation of
29 ozone⁴, another GHG and air pollutant.

30 Despite the critical importance of CH₄ for climate, the existing CH₄ observing network has
31 proven inadequate to constrain global, regional, and sectoral sources, and explain observed
32 trends and variation in atmospheric CH₄ over the last few decades. Therefore, there is a critical
33 need for CH₄ observations for constraining the strength and distribution of methane's sources,
34 including natural (e.g., wetlands) and anthropogenic (e.g., energy sector) ones. For instance,

35 much of the year-to-year variations in methane's global growth rate are likely from variations in
36 wetland emissions and part of the recent increasing trend in methane's growth rate may be
37 associated with increased energy extraction activities^{5,6}. An adequate CH₄ observing network is
38 necessary to monitor the interaction between the carbon cycle and climate change, such as the
39 potential release of CH₄ from stored carbon reservoirs (e.g., Arctic and boreal soils) and changes
40 in natural emissions. The current CH₄ observing network does not provide the necessary data to
41 understand and constrain methane's sources, such as from permafrost thaw, wetlands, which
42 challenges our ability to make confident projections of future climate. The importance of
43 measuring CH₄ is also reflected in the last National Research Council Decadal Survey for Earth
44 Science⁷ and the recent report by the Carbon Climate Workshop⁸.

45 Our current understanding of CH₄ distributions and processes is founded mostly on precise and
46 accurate ground-based, in-situ measurements from global monitoring networks^{9,10}. The location
47 and frequency of these measurements is, however, very sparse on a global scale and is even
48 sparser at high latitudes where the thawing Arctic permafrost is of particular concern. Large
49 quantities of organic carbon are stored in the Arctic permafrost and a warming climate can
50 induce drastic changes in carbon emissions and a subsequent positive feedback mechanism that
51 can significantly accelerate climate change¹¹.

52 Global measurements from satellites are available from passive optical sensors AIRS¹²,
53 SCIAMACHY^{13,14}, TES¹⁵, IASI¹⁶, and GOSAT¹⁷, but currently lack the required sensitivity to
54 derive regional CH₄ sources. Passive sensors measuring reflected sunlight are limited to sunlit
55 areas of the planet and their sensitivity falls off at low sun angles, increasing cloud cover, aerosol
56 scattering, and low surface reflectivity. Recent observations indicate that the thawing Arctic

57 permafrost is active even during the cold season¹⁸ highlighting the need for continuous sampling
58 at high latitudes even in the winter months.

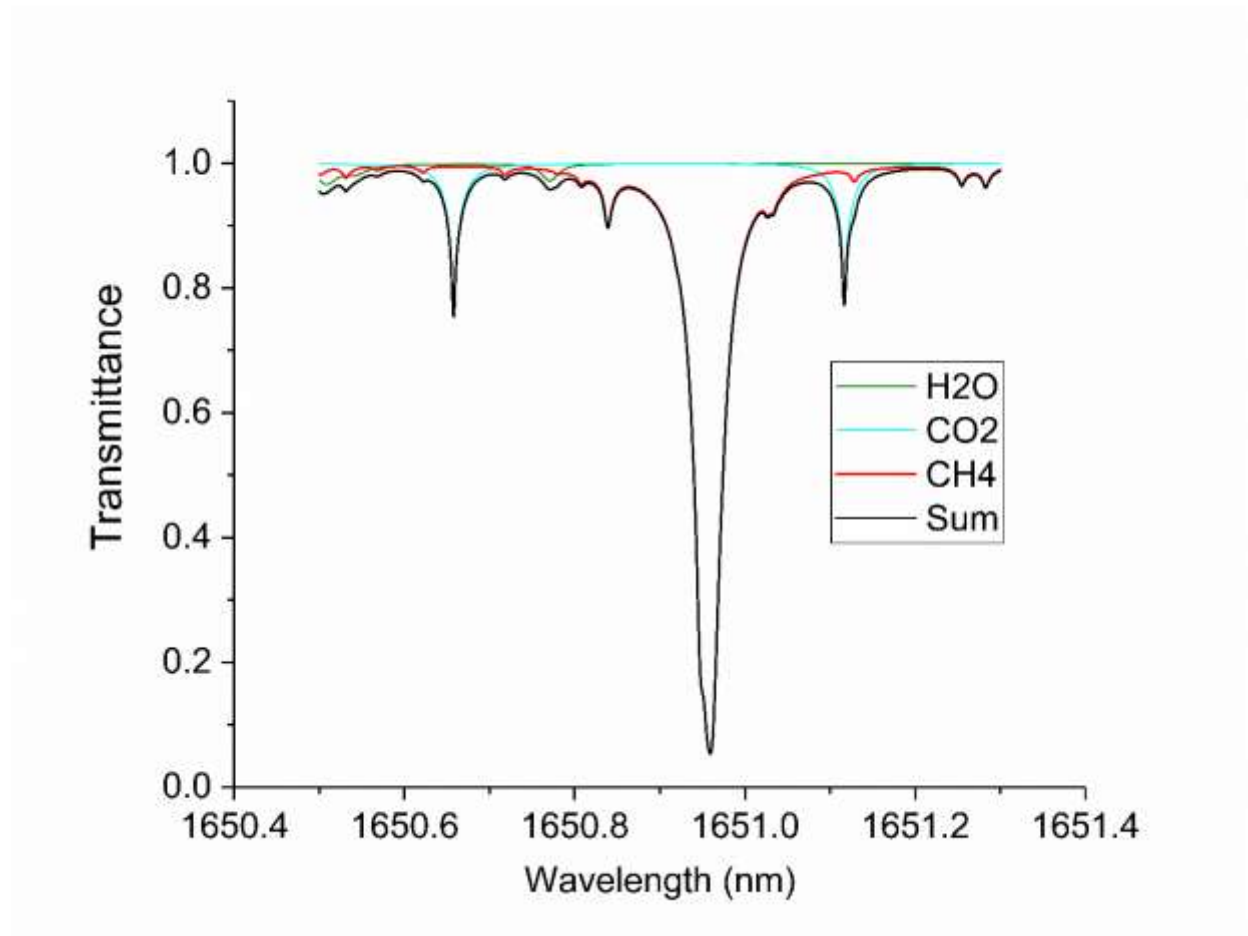
59 The benefit of active sensing missions is that they provide global CH₄ measurements where they
60 are really needed: in the absence of sunlight (i.e., at night and at high latitudes in all seasons), in
61 the presence of scattered or optically thin clouds and aerosols, over land and water surfaces, and
62 with higher accuracy and precision than currently available. Active measurements using laser
63 remote sensing technology will be a key step in obtaining measurements of CH₄ from orbit with
64 sufficient coverage, sampling, accuracy and precision to address key science questions. The
65 French Centre National d'Etudes Spatiales (CNES) in collaboration with the German Aerospace
66 Centre (DLR) are developing an active methane mission called MERLIN (Methane Remote
67 Sensing Lidar Mission) scheduled for launch in 2021^{19, 20}. The MERLIN mission targets an 8-36
68 ppbv relative random error in the methane column abundance with a 50 km horizontal resolution.
69 At NASA Goddard Space Flight Center (GSFC), we have been developing an active, airborne
70 lidar to measure atmospheric methane using Integrated Path Differential Absorption (IPDA) as a
71 precursor to a space mission to measure CH₄ from orbit.

72 **2 Instrument Description**

73 An IPDA lidar measures the absorption of laser pulses by a trace gas when tuned to a wavelength
74 coincident with an absorption line²¹⁻³¹. Using the instrument in a sounding (surface reflection)
75 mode which enables integrated column trace gas measurements from orbit with relatively modest
76 laser power.

77 The GSFC IPDA lidar uses a tunable, narrow-linewidth light source and a photon-sensitive
78 detector coincident with a CH₄ absorption at 1650.96 nm. The CH₄ spectrum at 1650.96 nm is
79 well suited for active remote sensing. The CH₄ line is mostly isolated from adjacent CO₂ lines

80 and there is very little water (H₂O) vapor interference. The MELRIN line at 1645.55 nm is less
81 suitable for our technique because it is interfered with by H₂O vapor at ~1645.47 nm and it is
82 wider than our line (~56 pm vs. ~36 pm), an important consideration because it increases the
83 tuning requirement for our laser transmitter. Fig. 1 shows the two-way atmospheric transmittance
84 spectrum around 1650.96 nm from a 400 km orbit using the 2008 HITRAN database³² and a US
85 standard atmosphere.



86

87 **Fig. 1.** Two-way atmospheric transmittance near 1650.96 nm a from a 400 km orbit using the 2008 HITRAN
88 database and a US standard atmosphere. The CH₄ line is mostly isolated from adjacent CO₂ and H₂O vapor lines.
89

90 Although in principle, only two wavelengths (“on” and “off” the line) are needed to determine
91 the transmittance through the atmospheric column, our technique uses multiple wavelengths to

92 probe the absorption feature. Using multiple wavelengths can reduce errors that may affect the
93 measurement precision³³, measure the spectral shift of the line with changing atmospheric
94 pressure³⁴, generate atmospheric backscatter profiles of the entire column³⁵, and enable retrievals
95 of trace gas mixing ratios above and below the planetary boundary layer³⁶.

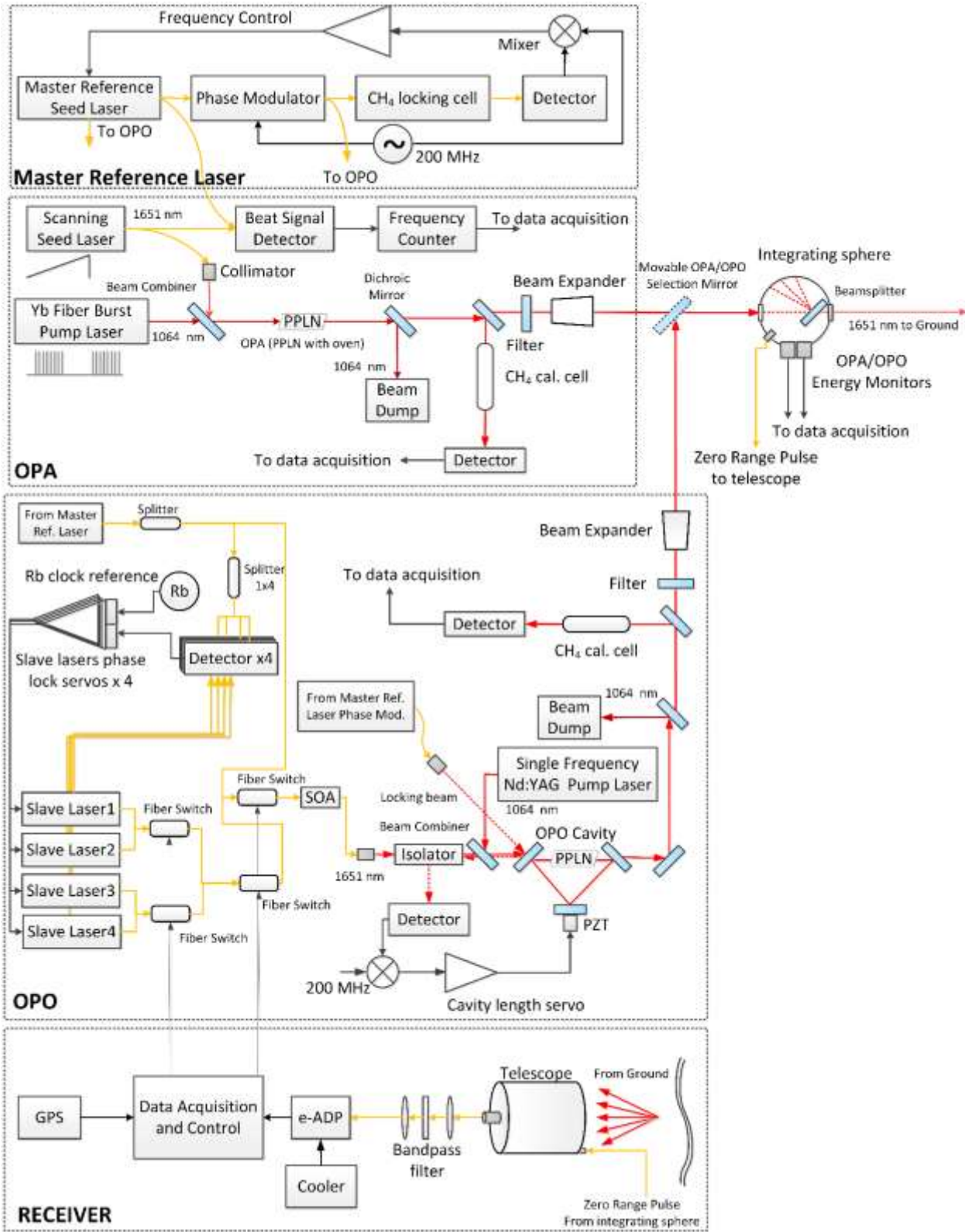
96 An early version of our instrument²⁵ flew in 2011. The major differences between the system in
97 ref. 25 and the new instrument are: 1) the detector: in 2011 we used a very low (<1%) quantum
98 efficiency (QE) photomultiplier tube (PMT) with very limited dynamic range. The new
99 instrument used an enhanced avalanche photodiode (e-ADP) with ~90% QE. 2) The type and
100 energy of the transmitter(s): In 2011, we used a low energy Optical Parametric Amplifier (OPA)
101 laser transmitter with pulse energy of ~10 μ J. The new airborne lidar used an OPA and an
102 Optical Parametric Oscillator (OPO) with pulse energies of ~25 μ J and ~250 μ J respectively. 3)
103 The opto-mechanical layout and data acquisition system were completely redesigned and
104 considerably improved. As a result, spurious effects such as etalon fringes were dramatically
105 reduced which improved the precision of the instrument.

106 Our new airborne IPDA lidar used two different laser transmitters. The first is an Optical
107 Parametric Amplifier (OPA) and the second is an Optical Parametric Oscillator (OPO). Only one
108 laser transmitter is used at a time by using a movable mirror to select the desired transmitter. A
109 simplified block diagram of our lidar is shown in Fig. 2 and is based on our previous work with
110 optical parametric generation³⁷.

111 The OPA, used 20 wavelengths, but was simpler to implement than the OPO, because it did not
112 require an optical resonator cavity, was easier to align and tune, and used only two seed lasers.
113 However, it is extremely difficult to scale the OPA energy to the level needed for space and still
114 maintain a narrow linewidth. Depending on the receiver size and other instrument parameters

115 we calculate that approximately 600 μJ is needed to obtain a measurement with a 0.5% precision.
116 The underlying reason for the wider linewidth is the large mismatch between the seed and pump
117 energies, which makes it very difficult to amplify the seed with the desired spectral
118 characteristics. If the seed laser power can be significantly scaled up and back-conversion can
119 be suppressed then it may be possible to achieve energies of 600 μJ out of the OPA with the
120 desired spectral characteristics.

121 In the OPO, narrow linewidth is achieved by using an optical resonator cavity, which also
122 enhances the energy of the non-linear conversion. Our OPO uses five wavelengths and a 1.2 mJ
123 GSFC-built solid-state pump laser with a triangular optical ring cavity. The OPO energy could
124 be scaled to space ($\sim 600 \mu\text{J}$) and maintain a narrow linewidth with a suitable higher energy pump
125 laser and improved optical design. However, the OPO currently requires a separate seed laser
126 and complex optical phase-lock loops for each wavelength used.



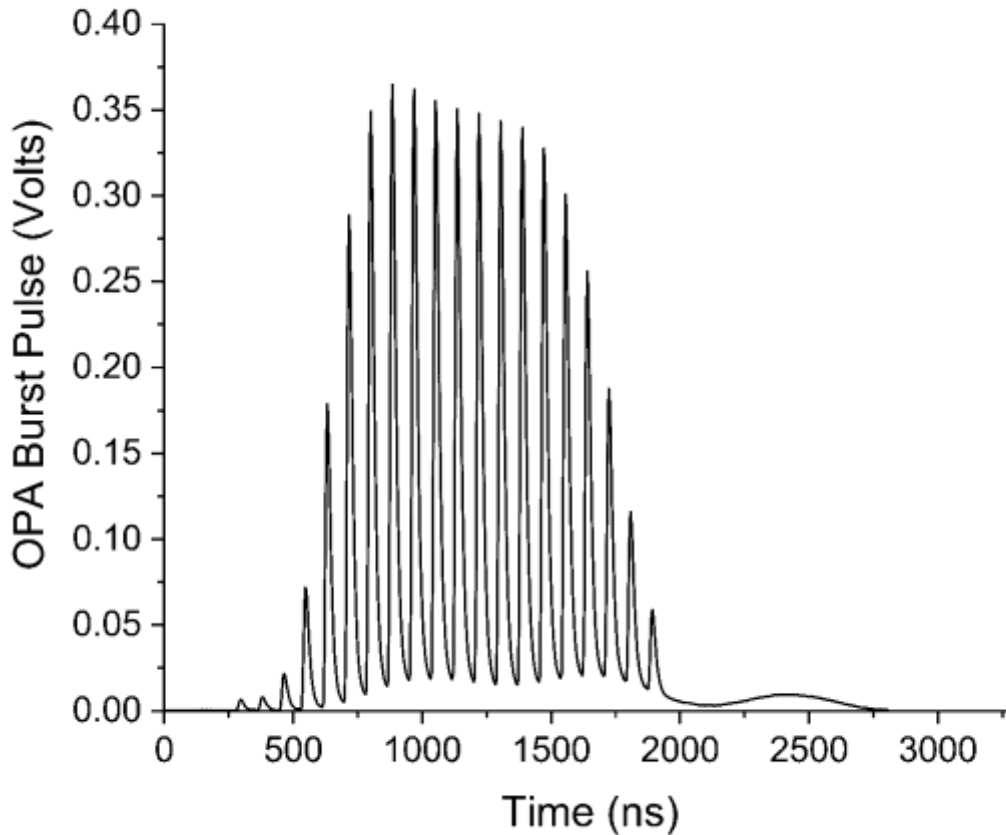
127

128
129

Fig. 2. Simplified functional block diagram of our IPDA lidar. The lidar can use one of two different laser transmitters using a movable selection mirror: An Optical Parametric Amplifier (OPA) or an Optical Parametric

130 Oscillator (OPO). The transmitters use DFB diode lasers for seed lasers but different pump lasers. Only one laser
131 transmitter is operating during flight.
132

133 The first transmitter option (OPA) consists of a magnesium oxide-doped periodically poled
134 Lithium Niobate (MgO:PPLN) crystal which is pumped by a pulsed single-frequency 1064 nm
135 laser and seeded by a continuous-wave (CW) 1650.96 nm laser diode. The pump laser is a
136 custom burst-mode Yb fiber laser from Fibertek Inc., based on a Master Oscillator Power
137 Amplifier (MOPA) configuration³⁸. The pump laser was optimized for high peak power and
138 generated 600 μJ in a burst pulse. Each burst pulse consists of twenty individual 3 ns pulses
139 separated by 85 ns with the individual pulse energies in the burst varying from 2 to 10 μJ . An
140 example of the OPA burst pulse is shown in Fig. 3.



141

142 **Fig. 3.** Example of temporal shape of the OPA burst pulse from the energy monitor detector showing individual
 143 pulses within the burst pulse.

144

145 The OPA output varies non-linearly with the peak power of the pump so the variation in the
 146 individual pump pulses resulted in very low conversion in the OPA of the low energy pulses.

147 The linewidth of the OPA was ~500 MHz. The pump laser was delivered with a bare, large
 148 mode area (LMA) fiber output that optimized the power output but was not suitable for flight.

149 Prior to our flights, we connectorized the output and the burst pulse energy was reduced to 350
 150 μJ per burst pulse.

151 Two distributed-feedback (DFB) CW diode lasers, a master reference and a scanning seed, from
 152 NEL America (NLK1U5FAAA), are used in the OPA. The wavelength of the master reference

153 laser is locked on the absorption peak at ~ 1650.96 nm using a 16.5 cm cell containing ~ 40 mbar
154 of CH_4 . The locking technique is the same for both the OPA and OPO, and is described by
155 Numata^{39, 40}. It is based on the technique used by Pound–Drever–Hall⁴¹ and is similar to the
156 technique used by Fix⁴². We estimate that the long-term drift of the master laser frequency is \sim
157 2 MHz, based on our experience with similar DFB seed lasers for CO_2 .

158 The scanning seed laser is tuned over the CH_4 line by rapidly scanning the laser current. The
159 beat signal between the master reference laser and the scanning seed laser is measured by a
160 frequency counter and recorded by the data acquisition system. The frequency of the beat signal
161 is converted into the OPA wavelengths in post-processing.

162 The scanning seed and pump laser beams are combined with a beam combiner and focused
163 through the PPLN crystal. The temperature of the PPLN crystal can be temperature-tuned to
164 optimize the phase matching at the seed wavelength. The unconverted pump beam at 1064 nm is
165 separated from the signal beam at 1650.96 nm using a dichroic mirror and directed into a beam
166 dump. A small part of the OPA beam at 1650.96 nm is also directed through an 8 cm reference
167 cell containing ~ 170 mbar of CH_4 for calibration purposes and a blocking filter prevents any
168 remaining 1064 nm radiation from exiting the aircraft. The main OPA output beam is directed
169 through a beam expander to reduce its divergence. The final output energy of the OPA
170 transmitter exiting the aircraft was approximately 25 μJ per burst pulse and 20 wavelengths were
171 used in each wavelength scan to sample the CH_4 lineshape.

172 The second transmitter (OPO) consists of another temperature controlled PPLN crystal inside a
173 three-mirror cavity. The temperature of the PPLN crystal can be temperature-tuned to optimize
174 the phase matching at the seed wavelength. The OPO is pumped by a pulsed single-frequency
175 1064 nm Nd:YAG laser and seeded by five CW DFB lasers at ~ 1650.96 nm.

176 The pump laser of the OPO is a custom-made GSFC single frequency Nd:YAG laser with a ~60
177 ns pulse width and maximum energy of 1.2 mJ per pulse at a 5 kHz repetition rate.

178 The same master reference seed laser used in the OPA is used for the OPO. Part of the phase-
179 modulated master reference beam (labelled “locking beam” in Fig. 2) is used to lock the OPO
180 cavity using a cavity length-control servo and a piezo electric transducer (PZT). Four additional
181 slave DFB diode lasers are offset-locked to the master reference laser by an integral number of
182 the OPO cavity free-spectral range (FSR) using the beat signal from four detectors and four
183 optical phase locked loop servos and a Rubidium frequency reference. Thus, the OPO samples
184 the CH₄ absorption at five wavelengths (one master and four slave). The wavelengths are
185 selected by switching fast (NanoSpeed™) 1x2 fiber optic switches made by Agiltron.

186 After exiting the OPO cavity the unconverted pump beam at 1064 nm is separated from the
187 signal beam at 1650.96 nm using a dichroic mirror and directed into a beam dump. After the
188 dichroic mirror, a small part of the OPA beam at 1650.96 nm is directed through a 5 cm CH₄
189 reference cell containing ~260 mbar of CH₄ for calibration purposes and a blocking filter
190 prevents any remaining 1064 nm radiation from exiting the aircraft. The main OPO output
191 beam is directed through a beam expander to reduce its divergence. The maximum output energy
192 of the OPA transmitter exiting the aircraft was approximately 250 μJ per pulse. The measured
193 linewidth of the OPO was less than 300 MHz but the measurement was limited by the resolution
194 of the Fabry-Perot etalon we used³⁹.

195 The divergence for both laser transmitters was ~150 μrad. Prior to exiting the aircraft through
196 the nadir port, a wedged beam splitter sends a small portion of the outgoing beams (~4 %) to an
197 8.9 cm diameter integrating sphere with two InGaAs detectors attached to one of its ports (one
198 for the OPA and one for the OPO). The detectors measure the outgoing energy monitor pulses

199 for the OPO or OPA and are digitized by the data acquisition system. The energy monitor pulses
200 are used to normalize the reflected pulses from the ground every 1/16 second in post processing.
201 In addition to the energy monitors, a multimode 200- μm core fiber is also connected to a port of
202 the integrating sphere and collects a small fraction of the outgoing laser energy. The multimode
203 fiber output is collimated and fed back into the receiver telescope and on focused on our
204 sensitive detector to provide a zero range pulse (or “start pulse”) for our ranging algorithm. The
205 time of flight from the zero range pulse to the reflected pulses from the ground is used to
206 determine the IPDA lidar range.

207 The laser pulses reflected from the ground are collected by a commercial 20 cm diameter
208 receiver telescope (Vixen VC200L) with an effective focal length of 2 m and are coupled into an
209 anti-reflection (AR) coated 600- μm core multi-mode fiber. The receiver field of view (FOV)
210 was 300 μrad . The receiver fiber output is collimated by a lens and directed through a 0.8 nm
211 (FWHM) band pass filter, and then focused onto a HgCdTe enhanced avalanche photodiode (e-
212 ADP) by DRS Technologies⁴³⁻⁴⁵. The detector is a 4x4-pixel array, with the pixel pitch being 80
213 μm with no gaps between pixels. The detector is operated at 80K and its electrical bandwidth is
214 ~ 7 MHz.

215 The signals from the frequency counter, reference cell (OPA or OPO), the energy monitor (OPA
216 or OPO), the zero range pulse, and ground return pulses are digitized by a National Instruments[©]
217 PXI-based data acquisition system containing a FlexRIO FPGA Module, a FlexRIO Digitizer
218 Adapter Module, a Timing and Synchronization Module, and a Global Positioning System (GPS)
219 module. All signals are averaged every 1/16 second and the files are time stamped by the GPS
220 time. Additional averaging can be performed in post-processing. The major parameters of the
221 airborne IPDA lidar are summarized in Table 1 below.

222

Table 1 Instrument Parameters

Parameter	OPA	OPO
Center Wavelength	1650.958 nm	1650.958 nm
Number of wavelengths used	20	5
Transmitter Energy/pulse	~25-30 μ J	~250 μ J
Transmitter Pulse rate	10 kHz	5 kHz
Transmitter divergence	~150 μ rad	~150 μ rad
Spectral Linewidth	~500 MHz	<300 MHz*
Number of seed lasers used	2	5
Pump laser	Burst mode Yb Fiber	Single pulse Nd:YAG
Pump laser energy	350 μ J	1.2 mJ
Receiver diameter	20 cm	20 cm
Receiver Field of view	300 μ rad	300 μ rad
Receiver band pass	0.8 nm (FWHM)	0.8 nm (FWHM)
Detector	4x4 HgCdTe e-ADP	4x4 HgCdTe e-ADP
Detector Pixel Pitch	80 μ m	80 μ m
Detector QE	~ 90%	~ 90%
Detector Temperature	80K	80K
Detector bandwidth	7 MHz	7 MHz
Averaging time	1/16 sec	1/16 sec

223 *Linewidth measurement limited by the resolution of the scanning Febry-Perot etalon used.

224 **3 Airborne Demonstration Results**

225 *3.1 Flights*

226 In late September 2015, the instrument was installed on the NASA DC-8 airborne laboratory,
227 based at Armstrong Flight Research Center Science Aircraft Integration Facility (SAIF) in
228 Palmdale, CA. The transceiver structure supported two small, vibration isolation, optical
229 benches for the OPO and OPA, the receiver telescope, and the transmit optics components. A
230 vibration isolation mechanism for the entire structure minimized the impact of aircraft vibrations.
231 The overall transceiver dimensions were approximately $0.9 \times 2.0 \times 0.8 \text{ m}^3$ and the total weight was
232 363 kg (Fig. 4). Two aircraft racks on either side of the transceiver structure held ancillary
233 instrumentation needed for the operation of the instrument (data acquisition and control
234 computers, detector, seed lasers, electronics, chillers for the pump lasers, etc.).



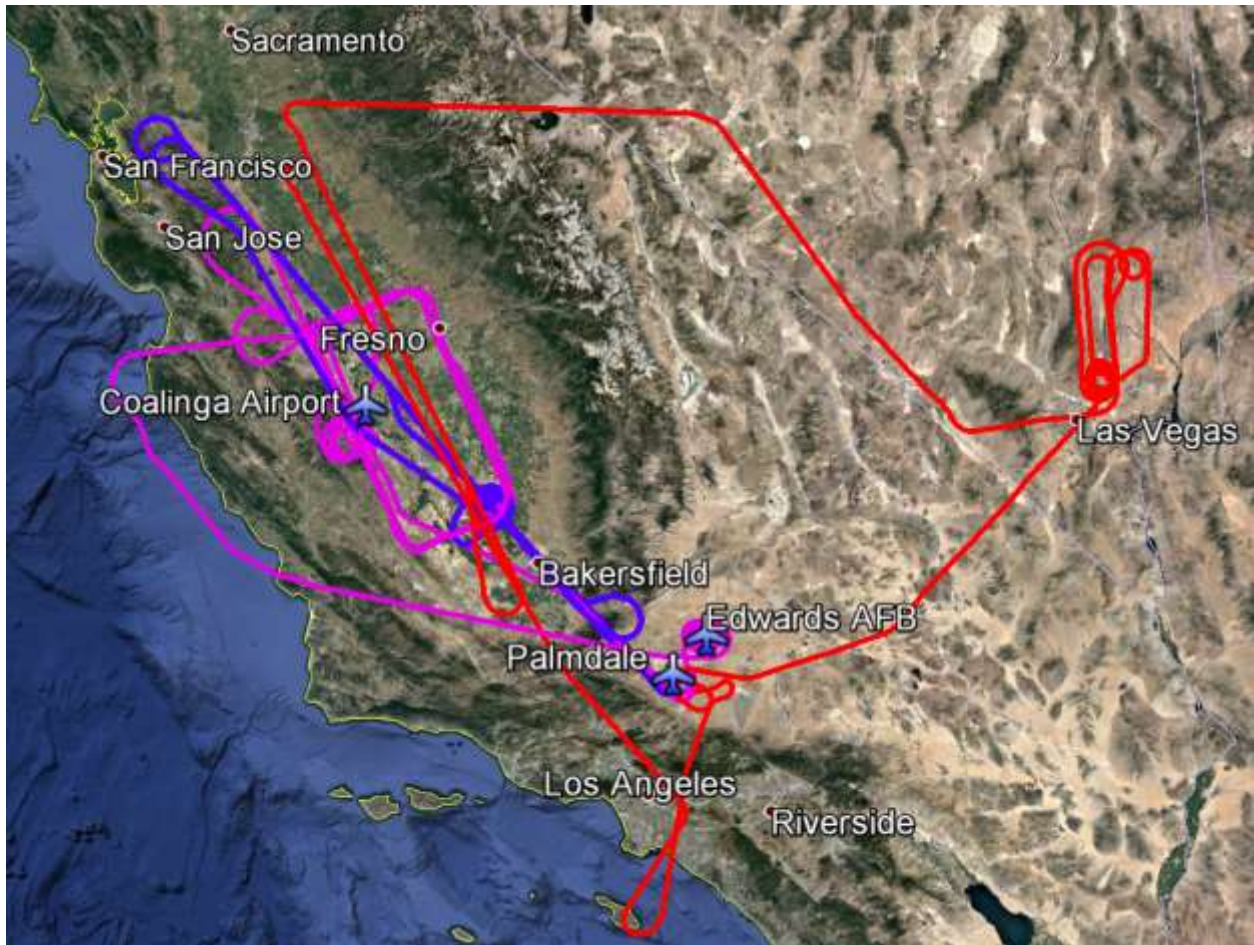
235

236 **Fig. 4.** The GSFC IPDA lidar installed on the NASA DC-8 airborne laboratory, in Palmdale, CA. The transceiver
237 structure supported two optical benches for the OPO and OPA, the receiver telescope, and the transmit optics
238 components. The overall transceiver dimensions were approximately $0.9 \times 2.0 \times 0.8 \text{ m}^3$ and the total weight was 363
239 kg. Two instruments racks on either side of the transceiver contained the control and data acquisition electronics.
240

241 A Picarro in-situ analyzer (Picarro G1301-m) measuring methane, carbon dioxide, and water
242 vapor using Wavelength-Scanned Cavity Ring Down Spectroscopy was also installed at a
243 different location in the aircraft to provide in-situ CH_4 reference measurements.

244 Three flights in the western United States were carried out in late September-early October 2015.
245 Flight planning was constrained by the limited number of flight hours available, the inclement
246 weather and aircraft maintenance issues. Each flight lasted about 4 hours and included several
247 segments at increasing altitudes from 2 to 13 km over varying topography, ground reflectivity
248 (including ocean), and atmospheric conditions. In addition, a spiral descent from ~ 13 km to near
249 the surface (~ 30 -300 m depending on Federal Aviation Administration flight clearances) was

250 included in the flight plan in order to sample the localized vertical profile of the CH₄ mixing
251 ratio and associated meteorological parameters (pressure, temperature, humidity, etc.) using the
252 Picarro in-situ sensor and the aircraft's data acquisition system. The IPDA lidar was always
253 turned off below 1 km above ground level (AGL) to comply with strict laser safety requirements.
254 Fig. 5 summarizes our flight paths in the western US. The flight tracks and locations were
255 chosen to minimize the transit flight time and targeted areas of potential CH₄ emission sources.



256 **Fig. 5** Flight tracks for the 2015 flights. Flight 1 (blue), Flight 2 (red), Flight 3 (magenta).
257
258

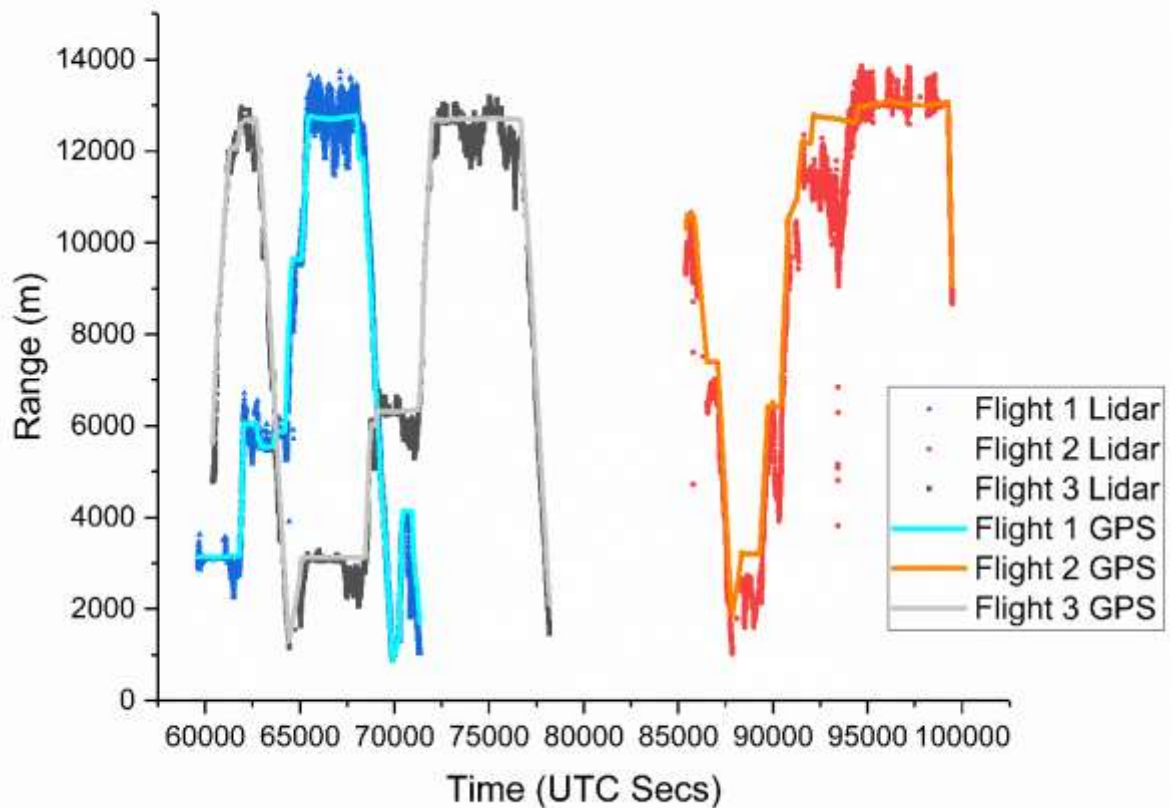
259 For the first two flights, we used the OPA transmitter and for the third flight, we used the OPO.
260 The first flight was mostly over the Central (San Joaquin) Valley of California. We flew on a
261 general south-north track, at three different altitudes at approximately 3.1, 5.9-6.0 km and 12.7

262 km. A large portion of the flight was in and over a dense cloud cover and the spiral descent
263 originally scheduled over Coalinga airport, CA was moved to approximately 40 km north of
264 Bakersfield, CA due to the weather conditions. The Coalinga airport was originally chosen due
265 to its proximity to a large feedlot.

266 The second flight targeted a large landfill approximately 30 km northeast of Las Vegas, NV.
267 After an initial pass at ~10 km and a subsequent spiral descent and low pass over the landfill at
268 ~300 m above ground level (AGL), two more flight segments were flown at 3.2 and 6.4 km.
269 Then we transited over to the Central Valley, CA where we did two high altitude north-south
270 flight segments at 12.7 and 13.1 km. Part of the Central Valley was completely covered by a
271 dense cloud cover during our flight.

272 The third flight was again over the Central Valley of California mostly due to adverse weather
273 conditions and flight restrictions at other candidate sites. We flew on a $\sim 75 \times 160$ km² rectangular
274 path centered on the Central Valley at three different altitudes: 3.1, 6.3 and 12.7 km. A spiral
275 descent and low pass (~30 m AGL) was performed over Coalinga airport. Following the high
276 altitude segment at 12.7 km, we flew over the Pacific Ocean and performed another spiral
277 descent over Edwards Air Force Base (AFB), CA prior to landing in Palmdale.

278 The flight altitude profiles (GPS altitude and IPDA lidar range vs. time) are shown in Fig. 6.



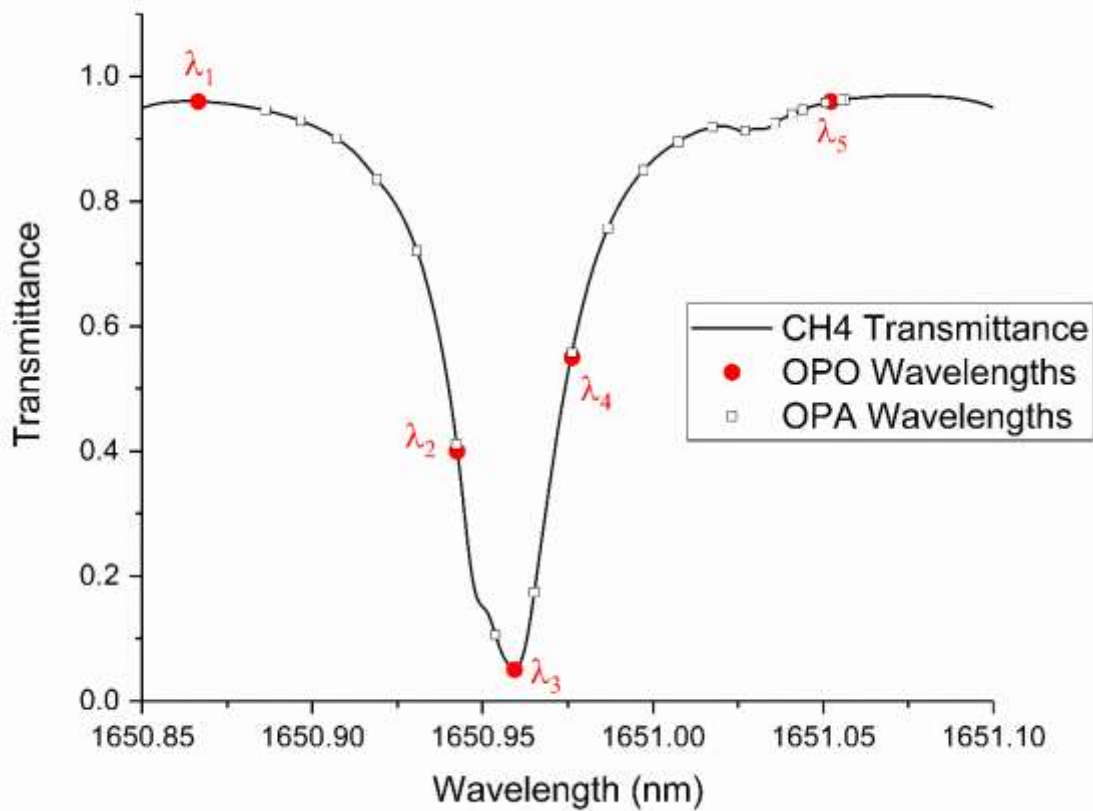
279

280 **Fig. 6.** Flight altitude (range) in m vs. time in UTC seconds since midnight as measured by the GPS receiver and our
 281 IPDA lidar for all three flights. The differences between the GPS and the IPDA lidar range are due to topography.
 282 The GPS measures the altitude above the mean sea level (or reference ellipsoid) but the IPDA lidar range is the
 283 altitude (range) above ground, which includes the topography.

284 *3.2 Retrievals*

285 Our retrieval algorithm uses a least squares fit to minimize the root mean squared error between
 286 the IPDA lidar measurements and the model prediction and is similar to the approach used by
 287 Abshire et.al.⁴⁶ in their CO₂ retrievals. The averaging time for the data acquisition system is
 288 1/16 sec but the data is further averaged in post processing in 1-sec intervals. First, the range
 289 (path length) from the aircraft to the surface is determined from the laser pulse time of flight
 290 (TOF) by correlating the first return pulse with the zero range pulse and measuring the time
 291 delay of the correlation peak, following the cross-correlation approach by Amediek⁴⁷. The

292 aircraft is equipped with a GPS antenna and a radar altimeter and we compare our lidar range
293 with the radar range to ensure that that only valid ground return pulses are used in the retrievals.
294 If only cloud returns are present, the data is not used in the analysis. However, there were many
295 occasions we had multiple returns from cumulus and cirrus clouds, and the ground. Segments
296 that did not contain enough valid ground returns due to the presence of clouds or other
297 instrument issues were excluded from the analysis. Generally when fewer than 50% ground
298 returns are present over a 1-second averaging period the data were not used. The algorithm then
299 estimates the column average of CH₄ transmittance of the atmospheric column by fitting the
300 integrated pulse returns from the surface at each wavelength, after normalization by the
301 transmitted pulse energy, the filter transmission, and other instrument calibrations. The
302 algorithm compares the experimental with the theoretically calculated transmittance values and
303 adjusts the fit parameters, including the mixing ratio, to minimize the fit error. The theoretical
304 calculations used a Voigt lineshape, the lineshape parameters from the HITRAN 2008 database
305 and line-by-line radiative transfer calculations⁴⁸. The impact of more complicated lineshape
306 functions and line mixing was not included in the calculations. However, recent spectroscopic
307 measurements by Delahaye⁴⁹ for the MERLIN line at 1645.55 nm suggest that differences of
308 1.5% up to 5% in the lineshape may arise if these effects are not taken into account. Fig. 7
309 shows a theoretical CH₄ lineshape from a 400 km altitude orbit with a US standard atmosphere,
310 and a comparison of the corresponding wavelength sampling by the OPA and OPO (20 vs. 5
311 wavelengths).

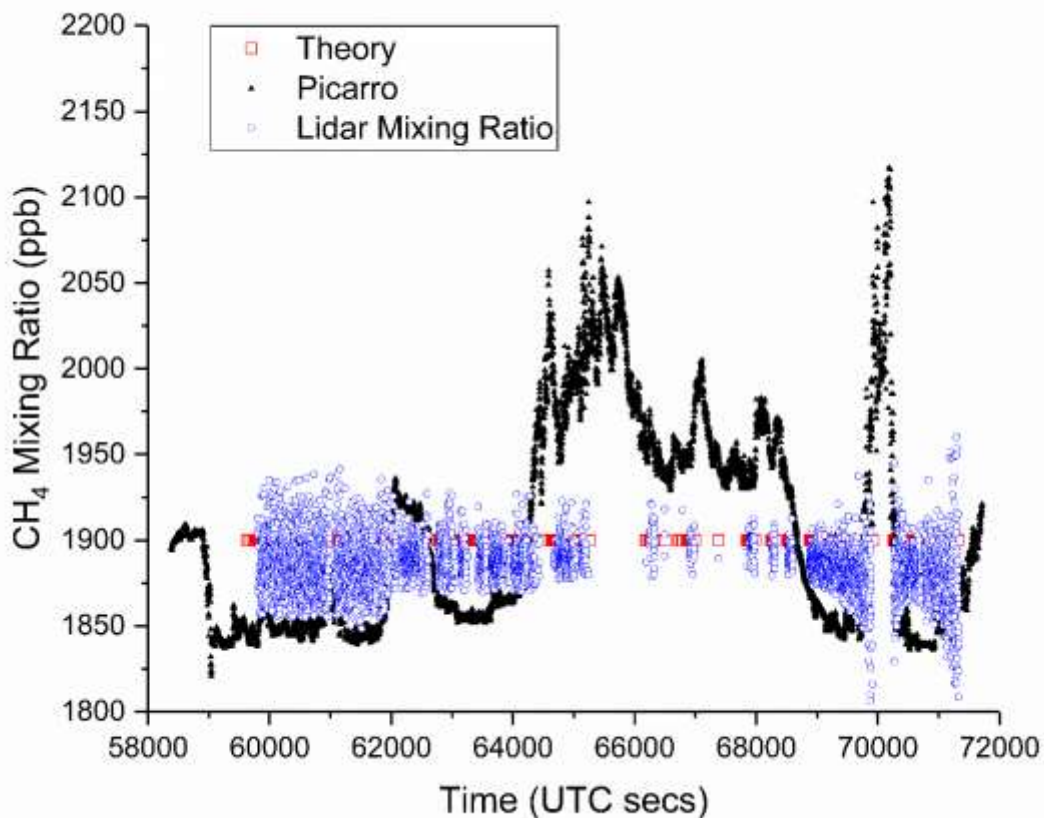


312 **Fig. 7** Theoretical CH₄ transmittance from a 400 km altitude with a US standard atmosphere and a comparison of
 313 the approximate wavelength sampling by the OPA (black open squares, 20 wavelengths) and OPO (red solid circles,
 314 5 wavelengths). For clarity, the OPO wavelengths are labeled λ_1 , λ_2 , λ_3 , λ_4 , λ_5 .
 315

316
 317 The meteorological data for the vertical profile of the atmosphere are obtained from the spiral
 318 descents, the Goddard Modeling and Assimilation Office (GMAO) Modern Era Retrospective -
 319 Analysis for Research and Applications (MERRA)⁵⁰ and the Goddard Earth Observing System
 320 Model, Version 5 (GEOS-5)⁵¹ with a sampling-interpolating interval of 1 second. The true CH₄
 321 mixing ratio profile over the entire flight path is of course, unknown. For simplicity, in our
 322 analysis the CH₄ mixing ratio used in the radiative transfer calculations was set at a constant
 323 1900 ppb. Although this value is clearly not an accurate estimate of the true mixing ratio for an
 324 entire flight, it is not very different from the column average values obtained by the in-situ
 325 spectrometer during our spirals and it provided a reasonable basis for estimating the precision,

326 but not necessarily the accuracy, of the IPDA lidar. In order to better assess the accuracy of an
327 IPDA lidar more frequent spirals and/or data from radiosondes are needed to infer the mixing
328 ratio profile over a flight path.

329 Fig. 8 shows the time series data of the in-situ CH_4 mixing ratio measured by the Picarro, the
330 theoretical CH_4 mixing ratio, set at 1900 ppb, and the CH_4 mixing ratio values obtained from our
331 retrieval algorithm for flight 1. There are obvious difference between the instrument retrievals
332 and those from the Picarro. That is to be expected since the Picarro is an in-situ measurement
333 and the lidar measures the column average.



334 **Fig. 8.** Time series data for flight 1 showing the in-situ CH_4 mixing ratio as measured by the Picarro, the theoretical
335 CH_4 mixing ratio (set at 1900 ppbv), and the CH_4 mixing ratio values by our retrieval algorithm. Outliers due to
336 instrument adjustments and clouds were filtered out.
337
338

339 There were multiple outliers in our retrievals that were filtered out. These were mainly due to
340 two factors: instrument adjustments and optically thick clouds. Due to aircraft vibrations and
341 changes in the cabin temperature and pressure, the OPA transmitter needed alignment
342 adjustments during flight to re-optimize its power. In addition, the wavelength locking circuitry
343 and instrumentation that locked and reported the wavelength of each laser pulse, by measuring
344 the frequency of the beat note between the reference laser and the scanning seed laser
345 wavelengths, would occasionally report erroneous values. The average wavelength values are
346 used if the reported wavelength value did not deviate more than ± 20 pm from the moving
347 average wavelength value. Finally, a significant part of the flight was over broken, optically
348 thick clouds. When all the outliers due to broken clouds and instrument adjustments were
349 filtered out, the agreement between the theoretical CH₄ mixing ratio, set at 1900 ppb, and the
350 retrieved CH₄ mixing ratio values was very good and the standard deviation of the retrieved CH₄
351 mixing ratio was 14.9 ppb or $\sim 0.8\%$ (14.9 ppb/1900 ppb). Assuming the column average CH₄
352 mixing ratio did not vary significantly this value represents a reasonable estimate of the
353 measurement precision of our IPDA lidar. Another good way to assess the IPDA lidar
354 performance is to plot the experimentally retrieved differential optical depth (DOD) vs. the
355 theoretical value. The theoretical and experimental DOD values are determined by the
356 difference in optical depth (OD) between the on wavelength interpolated at the wavelength
357 closest to the peak (~ 1650.965 nm) and the average value of the OD at the off wavelengths to the
358 left and right of the absorption (~ 1650.887 and ~ 1651.056 nm respectively). After removing all
359 the outliers due to laser power adjustments, erroneous wavelength values and broken clouds, the
360 DOD Lidar vs. DOD Theory linear fit (Fig. 9) had a slope of 0.98 and an offset of -0.007. The
361 R² value was 0.994.

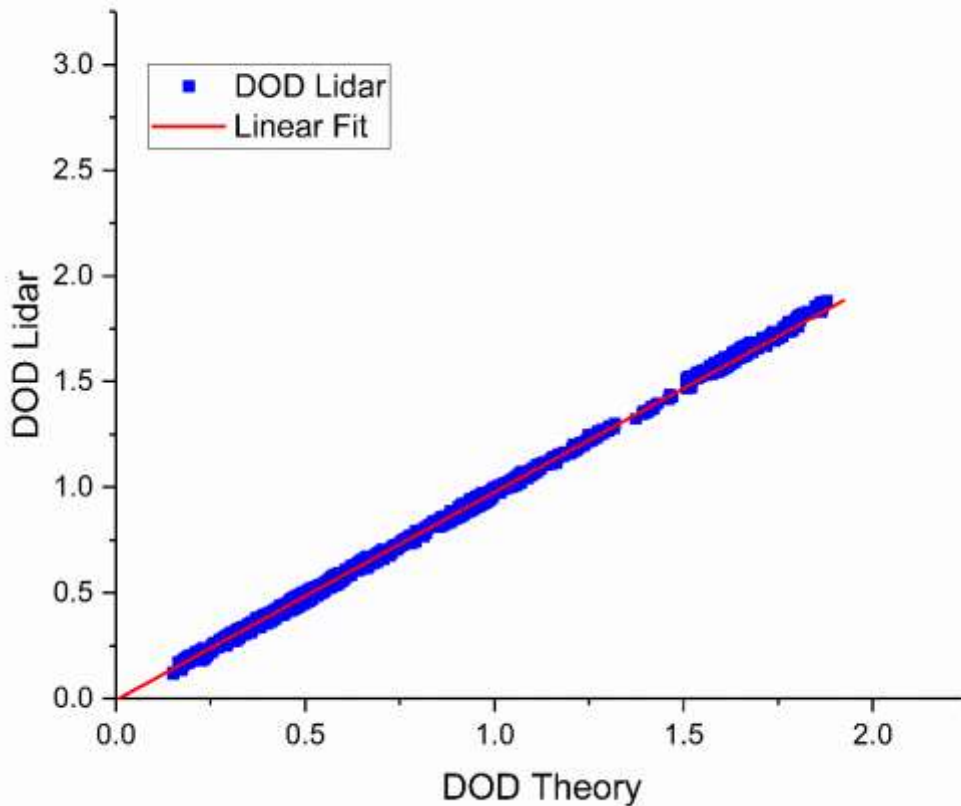


Fig. 9. Lidar DOD vs. Theoretical DOD for flight 1. The linear fit (without the outliers) had a slope of 0.98 and an offset of -0.007 and R^2 value was 0.994.

Fig. 10 Time series for flight 2 data showing the in-situ CH_4 mixing ratio as measured by the Picarro, the theoretical CH_4 mixing ratio (set at 1900 ppbv), and the CH_4 mixing ratio values by our retrieval algorithm. Outliers due to instrument adjustments and clouds were filtered out.

. The standard deviation of the retrieved CH_4 mixing ratio was 13.4 ppb or $\sim 0.7\%$ (13.4

ppb/1900 ppb). The DOD Lidar vs. DOD Theory linear fit for flight 2 had a slope of 0.998 and

an offset of -0.007 (Fig. 11. Lidar DOD vs. Theoretical DOD for flight 2. The linear fit (without

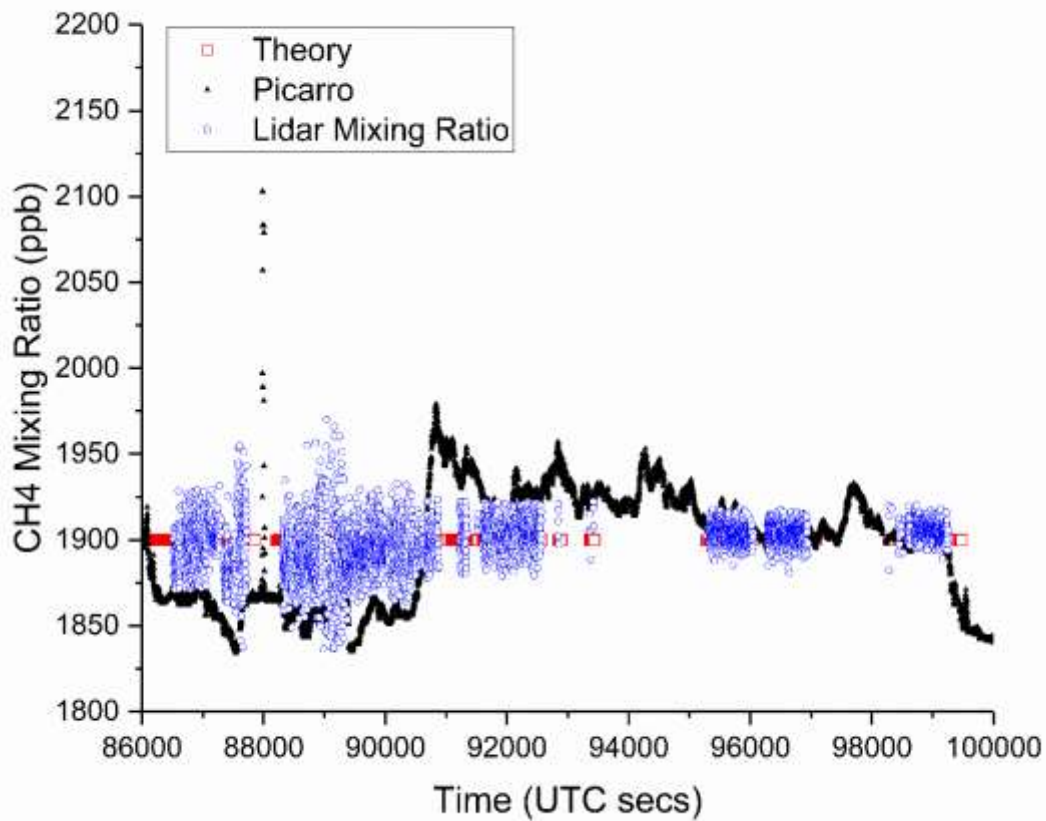
the outliers) had a slope of 0.998 and an offset of -0.007 and R^2 value was 0.990. The R^2 value

was 0.990. These values are consistent with flight 1 results indicating that when the instrument

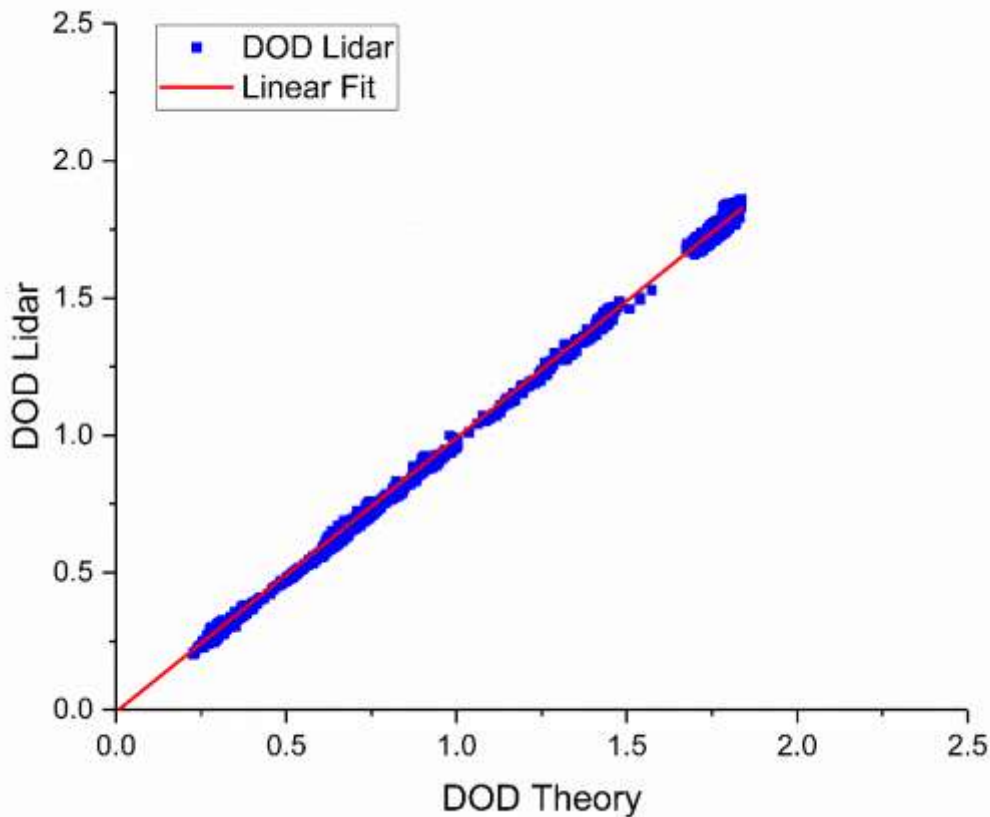
is operating properly (i.e. no adjustments are being made and no cloud interferences) it is capable

of measuring CH_4 mixing ratios with a 0.7-0.8 % precision. Obviously, the definition of the

377 instrument “operating properly” is subjective and in our case, it excluded sections of the flights
378 where the instrument needed adjustments. However, the current results provide “proof-of-
379 principle” evidence that a multi-wavelength IPDA lidar with an OPA can provide high enough
380 precision for meaningful science measurements from an airborne platform over a varying
381 topography and altitudes from 2 to 13 km.



382 **Fig. 10** Time series for flight 2 data showing the in-situ CH₄ mixing ratio as measured by the Picarro, the theoretical
383 CH₄ mixing ratio (set at 1900 ppbv), and the CH₄ mixing ratio values by our retrieval algorithm. Outliers due to
384 instrument adjustments and clouds were filtered out.
385



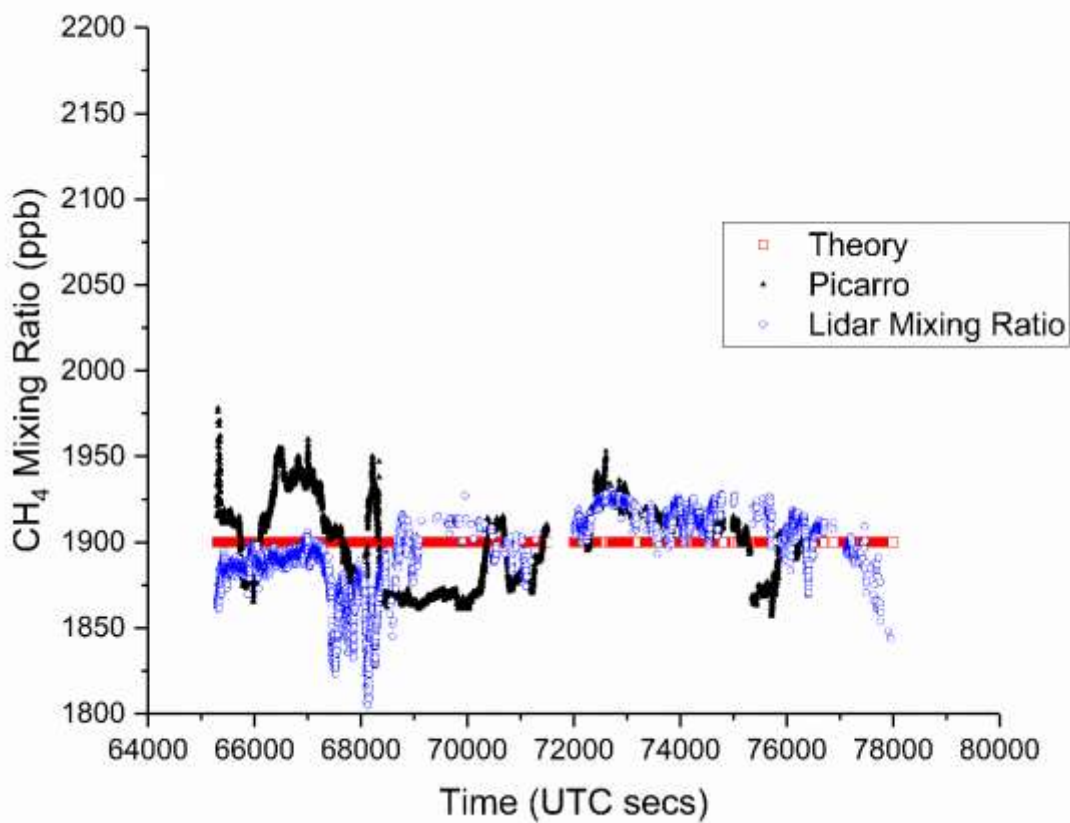
387
 388 **Fig. 11.** Lidar DOD vs. Theoretical DOD for flight 2. The linear fit (without the outliers) had a slope of 0.998 and an
 389 offset of -0.007 and R^2 value was 0.990.
 390

391 The last flight (flight 3) used the OPO as the laser transmitter. As shown in Table 1, the OPO
 392 used only five wavelengths vs. twenty for the OPA. Fewer wavelengths means that the lineshape
 393 is under-sampled and thus, it is more difficult to identify and remove any baseline slope and/or
 394 other artifacts in the data. The OPO transmitter also required adjustments during flight. In
 395 addition, the high OPO energy ($\sim 250 \mu\text{J}$) presented additional challenges. It saturated our
 396 detector especially at lower altitudes. Our initial plan to attenuate the received energy by
 397 restricting the receiver aperture size with a variable iris did not work for the flight configuration
 398 on the DC-8, even though we tested the idea successfully in the laboratory. The hardware that

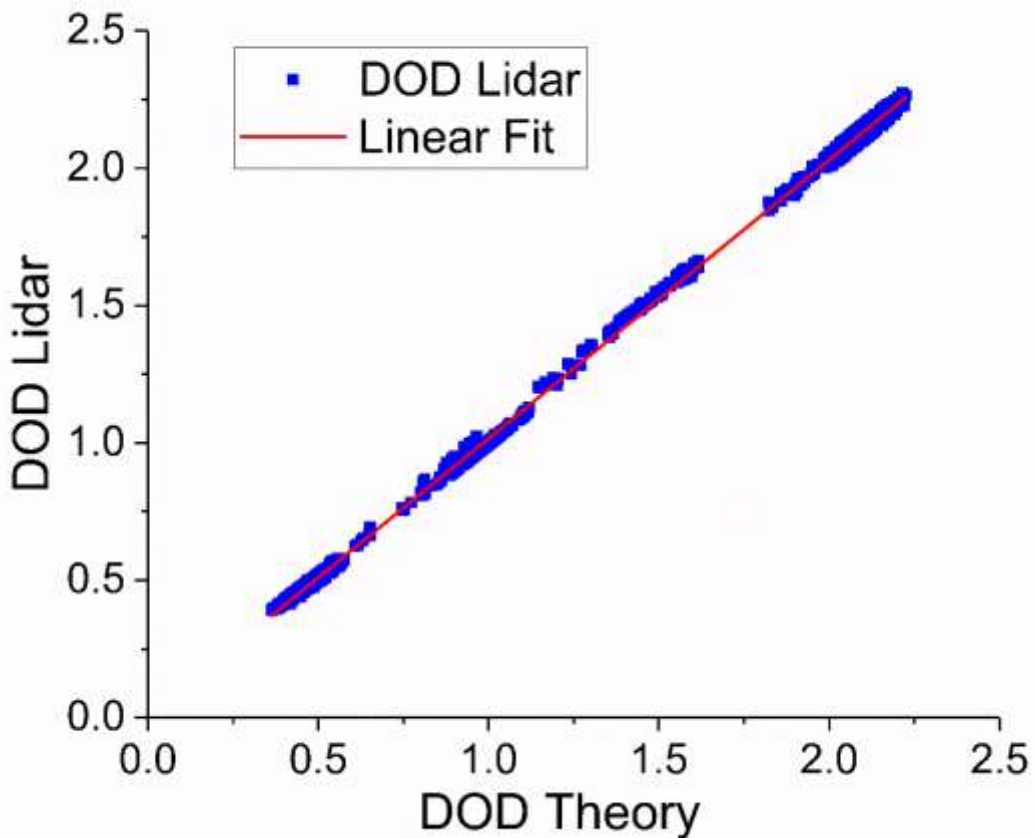
399 was used to restrict the receiver aperture size produced a large near field backscatter when
400 installed in the aircraft saturating and turning off the DRS detector. As a result, it could not be
401 used for flight and thus, the OPO energy was too high for the detector, especially for the low
402 altitude flight segment and over highly reflective surfaces. The detector gain had to be turned
403 down to its minimum value for part of the flight where the detector was presumed to be non-
404 linear. Our initial analysis showed a large discrepancy between the theoretical and experimental
405 DOD values. More importantly, we expected the discrepancy to be worse for the lower altitude
406 segment of the flight, where the detector was saturated and the gain was turned down to a
407 minimum. Contrary to our initial expectations, the DOD discrepancy was worse for the higher
408 altitude segment of the flight, where the detector was not saturated and operating in a linear
409 regime. Repeated post-flight calibrations of the DRS detector in the laboratory failed to uncover
410 any significant detector non-linearities within the digitizer dynamic range (1.23 V peak-peak)
411 that could account for the discrepancy we observed. For a given detector gain (bias) above
412 threshold, the detector is linear over at least two orders of magnitude and even when the detector
413 gain is set to its minimum value the results were repeatable and could be calibrated. Another
414 possible problem we uncovered in our post flight calibration was wavelength locking.
415 Wavelength 1 (λ_1) was initially reporting a “lock” status even though it was not always properly
416 locked on the correct wavelength. The problem was corrected quickly during flight (shortly after
417 the first spiral around 64000 secs UTC) but the data prior to the correction had to be discarded.
418 We hypothesized that the other wavelengths might have also experienced the same issue later in
419 the flight. Several post-flight calibrations in the laboratory with a high-resolution wavemeter
420 showed that the wavelength locking circuitry was operating properly and the circuitry was
421 reporting the wavelength values correctly. A detailed analysis of the OPO reference cell

422 indicated that the discrepancy was not due to the detector or the wavelength locking. The
423 discrepancy was traced to the fast fiber optic switches used to switch between the five OPO
424 wavelengths. The switches have a small amount of crosstalk and although the crosstalk was
425 initially measured to be relatively small, (~1-1.5%), the effect on the signal can be significant
426 especially at higher altitudes. Because of the crosstalk, the total signal received at each
427 wavelength has contributions from all five wavelengths. Wavelengths 1 and 5 (λ_1 and λ_5) are
428 “off line” and are not absorbed. Wavelengths 2, 3, 4 (λ_2 , λ_3 , λ_4) however, are absorbed and the
429 amount of absorption increases with altitude. As the altitude (absorption) increases the “on line”
430 wavelengths (λ_2 , λ_3 , λ_4) signals, have increasing contributions from the off line wavelengths (λ_1
431 and λ_5). Thus, a correction factor is needed to account for the crosstalk. The analysis of the
432 reference cell provided the initial evidence and estimate of the crosstalk correction factor.
433 Further refinement of the average correction factor at three different flight altitudes (3.1, 6.3 and
434 12.7 km) was obtained by ratioing the raw integrated pulse energies at wavelengths 1, 2, 4, and 5
435 to wavelength 3 and comparing the actual with the theoretical values. Obviously, the correction
436 factor values for different altitudes are just average estimates, not exact values and they vary
437 with altitude and topography. As the aircraft ascends or descends or the topography changes the
438 crosstalk factor will change. Furthermore, as the performance and gain of the OPO cavity
439 changes there is no guarantee that the crosstalk between wavelengths will remain fixed. The
440 crosstalk correction factor accounted for the observed discrepancy for the three constant flight
441 altitude segments of flight 3 (3.1, 6.3 and 12.7 km) and was applied to the analysis. Fig. 12
442 shows the time series data of the in-situ CH₄ mixing ratio from the Picarro, the theoretical CH₄
443 mixing ratio, set at 1900 ppb, and the retrieved CH₄ mixing ratio values for the three constant
444 flight altitude segments (3.1, 6.3 and 12.7 km) used in the analysis. When the outliers were

445 removed, the standard deviation of the retrieved CH₄ mixing ratio was 21.4 ppb or ~1.1 % (21.4
446 ppb/1900 ppb). The DOD Retrieval vs. DOD Theory linear fit (Fig. 13) had a slope of 1.01 and
447 an offset of -0.003. The R² value was 0.999. These values are comparable but slightly worse to
448 those obtained during flight 1 and 2 with the OPA but the number of outliers that were filtered
449 out was higher.
450



451 **Fig. 12** Time series for flight 3 data showing the in-situ CH₄ mixing ratio as measured by the Picarro, the theoretical
452 CH₄ mixing ratio (set at 1900 ppbv), and the CH₄ mixing ratio values by our retrieval algorithm.
453
454



455 **Fig. 13.** Lidar DOD vs. Theoretical DOD for flight 3. The linear fit had a slope of 1.01 and an offset of -0.003. The
 456 R^2 value was 0.999.
 457
 458

459 **4 Discussion**

460 The high accuracy and precision needed for CH₄ measurements poses several challenges for the
 461 IPDA lidar design. Currently the laser transmitter poses the greatest challenge. The transmitter
 462 must have narrow linewidth (<100 MHz), must be tunable to scan over the CH₄ absorption line
 463 (~250 pm), and must have high pulse energy. The exact energy requirement also depends on the
 464 detector quantum efficiency, receiver aperture size, and other instrument parameters. Our link
 465 margin calculations show that approximately 600 μJ is needed for space to achieve a 0.5%
 466 random error with a 1 m diameter telescope.

467 We have tried to address several potential error sources in our instrument design: Errors due to
468 cloud and aerosol scattering are minimized by our pulsed approach, which digitizes the entire
469 atmospheric column return and gates the returns from the ground. The IPDA lidar cannot
470 penetrate optically thick clouds. However, our ranging algorithm provides accurate knowledge
471 of the total pathlength minimizing the effect of multiple scattering and excluding returns from
472 clouds. In order to improve the accuracy of the measurement better knowledge of the
473 spectroscopic parameters of the CH₄ line and a more sophisticated lineshape function are needed.
474 The CH₄ line we used is actually comprised of multiple lines with different linestrengths and
475 temperature dependence.

476 There are obvious difference between the instrument retrievals and those from the Picarro. The
477 lidar values show less variation in the CH₄ mixing ratio, which is to be expected since the Picarro
478 is an in-situ measurement and the lidar measures the column average. The Picarro recorded a
479 significant increase in the in-situ CH₄ mixing ratio only for flight 1 despite the fact that we tried
480 to target landfills and other areas of increased CH₄ mixing ratios. No significant CH₄ mixing
481 ratio increase was observed near these areas by the Picarro for flights 2 and 3. The biggest
482 increase was observed during the spiral for flight 1 near the ground (around 7000 secs UTC in
483 Fig. 8) when the lidar was turned off to satisfy the laser safety requirements. The other big
484 increase was observed earlier in the flight (around 6600-6700 secs UTC in Fig. 8). The source of
485 that increase is unclear.

486 The predicted values (i.e. “truth”) to which our experimental data are fitted to, assumed a
487 constant CH₄ mixing ratio of 1900 ppb. The actual CH₄ mixing ratio profile over the entire flight
488 path is of course, unknown. Although 1900 ppb is clearly not an accurate estimate of the true
489 mixing ratio for an entire flight, it provided a reasonable basis for estimating the precision, but

490 not necessarily the absolute accuracy, of the IPDA lidar. In order to assess the accuracy of any
491 IPDA lidar multiple spirals and/or data from other sources such as radiosondes are needed to
492 measure the actual vertical distribution of CH₄ mixing ratio. Even then, differences and biases
493 will remain. Differences in the spectroscopic database (HITRAN 2012 vs. 2008), and effects
494 like line mixing and speed dependent profiles produce different results. Our incomplete
495 knowledge of the state of the atmosphere (pressure, temperature, and humidity) and the accuracy
496 of our meteorological model also contribute. Although the MERRA model was adequate for
497 these initial demonstration flights, in order to evaluate the IPDA lidar accuracy, better
498 knowledge and modeling of the state of the atmosphere and CH₄ vertical profiles at the local
499 level are needed. These can be obtained in future flights by increasing the frequency and
500 location of the spirals, including data from other instruments and radiosonde data if available.
501 Finally, lidar issues due to a variety of factors such as shot noise, ground reflectivity, speckle
502 noise, wavelength and power stability of the laser transmitter, etalon fringes, and in the case of
503 the OPO cross talk between wavelengths all contribute to biases in the measurement. With the
504 limited data obtained from these demonstration flights, we are not able to separate individual
505 bias sources. However, we did observe that the random noise was reduced by the expected
506 $1/\sqrt{t_{av}}$, where t_{av} is the averaging time, for up to ~5-10 secs. After ~5-10 secs, no improvement in
507 the noise statistics is observed.

508 The CH₄ IPDA lidar needs significant engineering improvements to increase its reliability. The
509 opto-mechanical design, laser transmitter stability, for both the OPA and OPO needs to be
510 considerably improved to reduce the effects of vibration, temperature and pressure. The locking
511 electronics and diagnostics for the seed lasers and OPO cavity also need to improve. The
512 isolation between OPO wavelengths needs to increase by at least an order of magnitude to

513 eliminate the need for crosstalk correction factors. All of these improvements are feasible if
514 proper engineering resources can be applied.

515 The OPA, which used 20 wavelengths, produced better fits, was simpler to implement than the
516 OPO because it did not require an optical resonator cavity, and was easier to align and tune.

517 However, it is extremely difficult to scale the OPA energy to that needed for space ($\sim 600 \mu\text{J}$
518 depending on the receiver size and other instrument parameters) and maintain a narrow
519 linewidth. The highest energy we obtained in the laboratory with our OPA was $290 \mu\text{J}$ using a
520 two-stage OPA, and the burst-mode Yb fiber laser amplified by a custom solid-state amplifier as
521 a pump. However, at high energies, the OPA output spectrum typically consists of sharp peak
522 near the seed wavelength and a broad side lobe, when the parametric gain is high. In that case,
523 we cannot clearly define the linewidth but it is generally too wide for accurate CH_4 IPDA lidar
524 measurements. In addition, for a space mission we are aiming for a simple and efficient single
525 stage - not a complex multi-stage - OPA based on quasi-phase matching (QPM). In this
526 configuration, we have observed that the OPA output linewidth does not fully converge to the
527 seed linewidth, giving wide side lobes, especially when pump and seed fluences are high and
528 low, respectively⁵². Similar side lobes were observed in seeded QPM-based OPA system for a
529 CO_2 lidar⁵³. Back-conversion and parametric amplification of the seed's side lobes are possible
530 causes. Complex OPA/OPG systems in other wavelength regions have been developed with a
531 narrow linewidth⁵⁴. However, it is difficult to predict how they can be implemented with a
532 multi-wavelength IPDA lidar for space because of their complexity. If the seed laser power can
533 be significantly scaled up then it may be possible to achieve energies of $600 \mu\text{J}$ out of the OPA
534 with a narrow linewidth. With the existing seed and pump laser technology, we do not see a path

535 to space for the OPA in the near future. However, it remains a viable transmitter for CH₄
536 measurements from an airborne platform.

537 In the OPO, narrow linewidth was achieved by using an optical resonator cavity, which also
538 enhances the energy of the non-linear conversion. Our 5-wavelength OPO uses a 1.2 mJ GSFC-
539 built solid-state pump laser and a triangular optical ring cavity. We have since replaced the
540 GSFC-built solid-state pump laser with a smaller, compact Yb fiber laser and redesigned the
541 OPO cavity to improve stability. In the laboratory we demonstrated energies of ~250 μJ at 5
542 kHz with a narrow (transform limited) linewidth. The OPO energy could be scaled to space but
543 it requires complex optical phase-lock loops and cavity control.

544 In recent years, resonantly pumped Erbium (Er) doped YAG, Er:YAG and Er:YGG, lasers,
545 which directly emit at 1645.5 and 1650.96 nm, respectively offer another option for a CH₄
546 transmitter. Using Er:YAG for CH₄ detection dates back to 1972⁵⁵ and recent successful
547 demonstration and commercialization of high power and high spectral brightness pump sources
548 have afforded the realization of resonant pumping of Er:YAG⁵⁶⁻⁵⁹ and Er:YGG^{60, 61}. The
549 emission cross-section of Er:YAG crystal is centered near 1645.3 nm and falls off rapidly at
550 1650.96 nm. It is near the MERLIN lines at 1645.55 nm which are relatively wide (~56 pm).
551 Our CH₄ line at 1650.96 nm is narrower (~36 pm) which makes fast tuning easier. Unfortunately,
552 Er:YAG cannot be used as a gain medium at 1650.96 nm but Er:YGG can be used as a potential
553 medium for lasing at that wavelength. Both materials are good candidates for a CH₄ laser
554 transmitter. Power scaling for both materials, multi-wavelength operation and tuning
555 considerations remain.

556 Our preliminary radiative transfer calculations show that both lines (Er:YAG at 1645.55 nm and
557 Er:YGG at 1650.96 nm) have similar temperature sensitivity and are well suited for space born

558 CH₄ measurements. Recent high accuracy spectroscopic measurements indicate that line mixing
559 effects in the Er:YAG 1645.55 nm line⁴¹ should also be taken into account. We expect similar
560 effects to be present for the Er:YGG line at 1650.96 nm.

561 **5 Summary**

562 We reported on an airborne demonstration of atmospheric CH₄ measurements with an Integrated
563 Path Differential Absorption (IPDA) lidar using an optical parametric oscillator (OPO) and
564 optical parametric amplifier (OPA) laser transmitter and sensitive avalanche photodiode detector.
565 The lidar measured the atmospheric CH₄ absorption at multiple, discrete wavelengths near
566 1650.96 nm. The instrument was deployed in 2015 aboard NASA's DC-8 airborne laboratory
567 and measured CH₄ mixing ratios from 2 km to 13 km. Relatively high precision measurements
568 of 0.7% to 1.1 % were demonstrated for all three flights however, many areas of improvement
569 remain. The stability and reliability of the laser transmitters need to improve considerably but the
570 basic measurement approach has been demonstrated. We are currently improving our airborne
571 instrument with better opto-mechanical design and compact, more stable laser transmitters. We
572 hope to fly again in the near future when the next opportunity arise.

573 **Acknowledgements**

574 The authors would like to acknowledge the generous support by the Earth Science Technology
575 Office (ESTO) Advanced Component Technology Program (ACT-13) and the GFSC Internal
576 Research and Development (IRAD) Program. The authors would like to thank Dr. Piers Sellers,
577 who passed away in December 2016, Ms. Lisa Callahan, and Dr. Matt McGill, for their
578 unwavering support of our lidar development and flight demonstration. The authors would also
579 like to thank Dr. Graham Allan and Dr. James Abshire for valuable discussions and

580 consultations. The authors would also like to express their appreciation to the DC-8 flight
581 operations team at the Science Aircraft Integration Facility in Palmdale, CA.

582

583

584

585

586

587

588

589 **References**

- 590 1. Intergovernmental Panel on Climate Change, *IPCC Fifth Assessment Report*, Cambridge Univ.
591 Press, Cambridge, U. K. and New York. (2013).
- 592 2. Saunois, Marielle, Philippe Bousquet, Ben Poulter, Anna Peregon, Philippe Ciais, Josep G. Canadell,
593 Edward J. Dlugokencky et al. "The global methane budget 2000-2012." *Earth System Science Data* 8,
594 **no. 2**, 697, (2016).
- 595 3. Trends in Atmospheric Methane, https://www.esrl.noaa.gov/gmd/ccgg/trends_ch4/, accessed on May
596 4th 2017.
- 597 4. Fiore, A. M., D. J. Jacob, B. D. Field, D. G. Streets, S. D. Fernandes, and C. Jang, "Linking ozone
598 pollution and climate change: The case for controlling methane", *Geophys. Res. Lett.*, **29** (19), 1919,
599 doi:10.1029/2002GL015601, 2002.
- 600 5. Franco, B., E. Mahieu, L. Emmons, Z. Tzompa-Sosa, E. Fischer, K. Sudo, B. Bovy, S. Conway, D.
601 Griffin, J. Hannigan, K. Strong, and K. Walker (2016), "Evaluating ethane and methane emissions
602 associated with the development of oil and natural gas extraction in North America", *Environ. Res.*
603 *Lett.*, **11.4** (2016).
- 604 6. Turner, A. J., D. J. Jacob, J. Benmergui, S. C. Wofsy, J. D. Maasakkers, A. Butz, O. Hasekamp, and
605 S. C. Biraud (2016), "A large increase in U.S. methane emissions over the past decade inferred from
606 satellite data and surface observations", *Geophys. Res. Lett.*, 43, 2218–2224, (2016).
607 doi:10.1002/2016GL067987.
- 608 7. National Research Council Decadal Survey: *Earth Science and Applications from Space: National*
609 *Imperatives for the Next Decade and Beyond*, National Academic Press, 2007.
- 610 8. Schimel, David, et al. "Observing the carbon-climate system." *arXiv preprint arXiv:1604.02106*
611 (2016).

- 612 9. Dlugokencky, E.J.; Steele, L.P., Lang, P.M., Masarie, K. A., “Atmospheric Methane at Mauna-Loa and
613 Barrow Observatories - Presentation and Analysis of In-Situ Measurements”, *J. Geophys. Res.*, **100**,
614 23103-23113, (1995). DOI: 10.1029/95JD02460.
- 615 10. Prinn, R. G., et al. (2000), “A history of chemically and radiatively important gases in air deduced
616 from ALE/GAGE/AGAGE”, *J. Geophys. Res.*, **105** (D14), 17751– 17792, (2000).
- 617 11. Schuur, E.A.G., McGuire, A.D., Schädel, C., Grosse, G., Harden, J.W., Hayes, D.J., Hugelius, G.,
618 Koven, C.D., Kuhry, P., Lawrence, D.M. and Natali, S.M., “Climate change and the permafrost
619 carbon feedback”. *Nature*, **520** (7546), pp.171-179, (2015).
- 620 12. Coheur, P.F., Xiong, X., C. D. Barnet, Q. Zhuang, T. Machida, C. Sweeney, and P. K. Patra, “Mid-
621 upper tropospheric methane in the high Northern Hemisphere: Spaceborne observations by AIRS,
622 aircraft measurements, and model simulations”, *J. Geophys. Res.*, **115**, D19309, (2010).
623 doi:10.1029/2009JD013796
- 624 13. Buchwitz, M., R. De Beek, J. P. Burrows, H. Bovensmann, T. Warneke, J. Notholt, J. F. Meirink, A.
625 P. H. Goede, P. Bergamaschi, S. Körner, M. Heimann, A. Schulz, "Atmospheric methane and carbon
626 dioxide from SCIAMACHY satellite data: initial comparison with chemistry and transport models",
627 *Atmos. Chem. Phys.*, **5**, 941–962, (2005).
- 628 14. Bergamaschi, P., Frankenberg, C., Meirink, J.F., Krol, M.C., Dentener, F.J.; Wagner, T., Platt, U.,
629 Kaplan, J.O., Körner, S.; Heimann, M.; Dlugokencky, E.J.; Goede, A. De, "Satellite cartography of
630 atmospheric methane from SCIAMACHY on board ENVISAT: 2. Evaluation based on inverse model
631 simulations", *Journal of Geophysical Research-Atmospheres*, Volume: **112**, pp. D02304/1-
632 D02304/26, (2007).
- 633 15. Wecht, K. J., Jacob, D. J., Wofsy, S. C., Kort, E. A., Worden, J. R., Kulawik, S. S., Henze, D. K.,
634 Kopacz, M., and Payne, V. H., “Validation of TES methane with HIPPO aircraft observations:
635 implications for inverse modeling of methane sources”, *Atmos. Chem. Phys.*, **12**, 1823-1832,
636 doi:10.5194/acp-12-1823-2012, (2012).

- 637 16. August, T., Klaes, D., Schlüssel, P., Hultberg, T., Crapeau, M., Arriaga, A., O'Carroll, A., Coppens,
638 D., Munro, R., Calbet, X., "IASI onMetop-A: Operational Level 2 retrievals after five years in orbit",
639 Journal of Quantitative Spectroscopy & Radiative Transfer **113**, 1340–1371, (2012).
- 640 17. Yokota, T., Y. Yoshida, N. Eguchi, Y. Ota, T. Tanaka, H. Watanabe, and S. Maksyutov, "Global
641 Concentrations of CO₂ and CH₄ Retrieved from GOSAT: First Preliminary Results", SOLA, Vol. **5**,
642 160–163, (2009). doi:10.2151/sola.2009–041
- 643 18. Zona, Donatella, Beniamino Gioli, Róisín Commane, Jakob Lindaas, Steven C. Wofsy, Charles E.
644 Miller, Steven J. Dinardo et al. "Cold season emissions dominate the Arctic tundra methane budget."
645 *Proceedings of the National Academy of Sciences* **113**, no. 1, 40-45, (2016).
- 646 19. Stephan, C., M. Alpers; B. Millet; G. Ehret; P. Flamant; C. Deniel, "MERLIN: a space-based
647 methane monitor", "Lidar Remote Sensing for Environmental Monitoring XII. Proceedings of the
648 SPIE, Volume 8159, pp. 815908-815908-15, (2011).
- 649 20. Kiemle, M. Quatrevalet, G. Ehret, A. Amediek, A. Fix, and M. Wirth, "Sensitivity studies for a space-
650 based methane lidar mission", Atmos. Meas. Tech. Discuss., 4, 3545–3592, 2011.
- 651 21. Measures, R., *Laser Remote Sensing*, Chapter 7, John Wiley & Sons, New York, 1984
- 652 22. Abshire, J.B., H. Riris, C. Weaver, J. Mao, G. Allan, W. Hasselbrack, and E. Browell, "Airborne
653 measurements of CO₂ column absorption and range using a pulsed direct-detection integrated path
654 differential absorption lidar," Appl. Opt. 52, 4446-4461 (2013).
- 655 23. Ehret, G., Kiemel, C., Wirth W., Amediek, A., et.al, "Space-borne remote sensing of CO₂, CH₄, and
656 N₂O by integrated path differential absorption lidar: a sensitivity analysis", Appl. Phys. B 90, 593-
657 608, (2008).
- 658 24. A. Amediek, Fix, A., Wirth, M., Ehret, G., "Development of an OPO system at 1.57 μm for integrated
659 path DIAL measurement of atmospheric carbon dioxide", Appl. Phys. B **92**, 295–302, DOI:
660 10.1007/s00340-008-3075-6, (2008).

- 661 25. Riris, H., K. Numata, S. Li, S. Wu, A. Ramanathan, M. Dawsey, J. Mao, R. Kawa, and J. Abshire,
662 "Airborne measurements of atmospheric methane column abundance using a pulsed integrated-path
663 differential absorption lidar," *Appl. Opt.* **51**, 8296-8305 (2012).
- 664 26. Riris, H., M. Rodriguez, G.R. Allan, W. Hasselbrack, J. Mao, M. Stephen, J. Abshire, "Pulsed
665 airborne lidar measurements of atmospheric optical depth using the Oxygen A-band at 765 nm,"
666 *Applied Optics*, **52**(25), 6369-6382 (2013).
- 667 27. Spiers, Gary D., et al. "Atmospheric CO₂ measurements with a 2 μm airborne laser absorption
668 spectrometer employing coherent detection." *Applied Optics* **50**.14, 2098-2111, (2011).
- 669 28. Dobler, Jeremy T., et al. "Atmospheric CO₂ column measurements with an airborne intensity-
670 modulated continuous wave 1.57 μm fiber laser lidar." *Applied Optics* **52**.12, 2874-2892, (2013).
- 671 29. Amediek, A., G. Ehret, A. Fix, M. Wirth, C. Büdenbender, M. Quatrevalet, C. Kiemle, and
672 C. Gerbig, "CHARM-F-a new airborne integrated-path differential-absorption lidar for
673 carbon dioxide and methane observations: measurement performance and quantification of
674 strong point source emissions," *Appl. Opt.* **56**, 5182-5197 (2017).
- 675 30. Fix, Andreas, Axel Amediek, Christian Büdenbender, Gerhard Ehret, Mathieu Quatrevalet,
676 Martin Wirth, Jens Löhring et al., "Development and first results of a new near-ir airborne
677 greenhouse gas lidar", *Optics and Photonics for Energy and the Environment*, pp. EM3A-3,
678 *Optical Society of America*, (2015).
- 679 31. Amediek, Axel, Gerhard Ehret, Andreas Fix, Martin Wirth, M. Quatrevalet, C. Büdenbender,
680 C. Kiemle, J. Loehring, and C. Gerbig. "First airborne IPDA lidar measurements of methane
681 and carbon dioxide applying the DLR greenhouse gas sounder CHARM-F", *AGU Fall*
682 *Meeting Abstracts*, (2015).
- 683 32. Rothman, L. S., et al. "The HITRAN 2008 molecular spectroscopic database." *Journal of Quantitative*
684 *Spectroscopy and Radiative Transfer*, **110**, 9, 533-572, (2009).

- 685 33. Chen, Jeffrey R., Kenji Numata, and Stewart T. Wu. "Error reduction in retrievals of atmospheric
686 species from symmetrically measured lidar sounding absorption spectra." *Optics express* **22.21**,
687 26055-26075, (2014).
- 688 34. Ramanathan, A., Jianping Mao, Graham R. Allan, Haris Riris, Clark J. Weaver, William E.
689 Hasselbrack, Edward V. Browell, James B. Abshire, "Spectroscopic measurements of a CO₂
690 absorption line in an open vertical path using an airborne lidar," *Applied Physics Letters*, **103**, 214102
691 (2013), DOI:<http://dx.doi.org/10.1063/1.4832616>
- 692 35. Allan, G. R., H. Riris, W. Hasselbrack, M. Rodriguez, A. Ramanathan, X. Sun, J. Mao, and J. B.
693 Abshire. "Atmospheric Backscatter Profiles at 765nm and 1572nm from Pulsed Lidar Measurements
694 of CO₂ and O₂ Column Absorption from the 2013 ASCENDS Flight Campaign." *AGU Fall Meeting*
695 *Abstracts*, **vol. 1**, p. 0211, (2013).
- 696 36. Ramanathan, Anand K., Jianping Mao, James B. Abshire, and Graham R. Allan. "Remote sensing
697 measurements of the CO₂ mixing ratio in the planetary boundary layer using cloud slicing with
698 airborne lidar." *Geophysical Research Letters* **42**, no. 6, 2055-2062, (2015).
- 699 37. Numata, K., Riris, H., S. Li, S. Wu, S. R. Kawa, M. Krainak, J. Abshire, "Ground demonstration of
700 trace gas lidar based on optical parametric amplifier", *Journal of Applied Remote Sensing*, **Vol. 6**,
701 063561-1, (2012).
- 702 38. Engin, Doruk, Ibraheem Darab, John Burton, Jean-Luc Fournon, Frank Kimpel, Brian Mathason,
703 Shantanu Gupta, and Mark Storm. "Highly-efficient, high-energy pulse-burst Yb-doped fiber laser
704 with transform limited linewidth." In *SPIE Defense+ Security*, pp. 908112-908112. International
705 Society for Optics and Photonics, (2014).
- 706 39. Numata, K., Riris, H., Wu, S., "Fast-switching methane lidar transmitter based on a seeded optical
707 parametric oscillator", *Applied Physics B*, **116**, 4, 959-966, (2014).
- 708 40. Numata, Kenji, Jeffrey R. Chen, and Stewart T. Wu. "Precision and fast wavelength tuning of a
709 dynamically phase-locked widely-tunable laser." *Optics express* **20.13**, 14234-14243, (2012).

- 710 41. Drever, R.W.P., J.L. Hall, F.V. Kowalski, J. Hough, G.M. Ford, A.J. Munley, H. Ward, *Appl. Phys.*
711 *B*, **31**, 97–105, (1983).
- 712 42. Fix, Andreas, Renaud Matthey, Axel Amediek, Gerhard Ehret, Florian Gruet, Christoph Kiemle,
713 Volker Klein, Gaetano Mileti, Joao Pereira do Carmo, and Mathieu Quatrevalet, "Investigations on
714 frequency and energy references for a space-borne integrated path differential absorption lidar",
715 *Proceedings of the International Conference on Space Optics*, **vol. 10**, (2014).
- 716 43. Beck, Jeff, et al. "A highly sensitive multi-element HgCdTe e-APD detector for IPDA lidar
717 applications." *Journal of Electronic Materials* **43.8**, 2970-2977, (2014).
- 718 44. Sun, Xiaoli, James B. Abshire, and Jeffrey D. Beck. "HgCdTe e-APD detector arrays with
719 single photon sensitivity for space lidar applications." *SPIE Sensing Technology+*
720 *Applications*. International Society for Optics and Photonics, (2014).
- 721 45. Sun, Xiaoli, James B. Abshire, Jeffrey D. Beck, Pradip Mitra, Kirk Reiff, and Guangning
722 Yang. "HgCdTe avalanche photodiode detectors for airborne and spaceborne lidar at infrared
723 wavelengths." *Optics Express* **25**, **14**, 16589-16602, (2017).
- 724 46. Abshire, J.B., Ramanathan, A.; Riris, H.; Mao, J.; Allan, G.R.; Hasselbrack, W.E.; Weaver, C.J.;
725 Browell, E.V. "Airborne Measurements of CO₂ Column Concentration and Range Using a Pulsed
726 Direct-Detection IPDA Lidar," *Remote Sensing* **2014**, **6**, 443-469, (2014)
- 727 47. Amediek, A., X. Sun, and J. B. Abshire, "Analysis of Range Measurements from a Pulsed Airborne
728 CO₂ Integrated Path Differential Absorption Lidar", *Transactions on Geoscience and Remote*
729 *Sensing*, **51**, No. 5, (2013).
- 730 48. Clough, S.A. and M.J. Iacono, M.I., "Line-by-line calculations of atmospheric fluxes and
731 cooling rates. 2: Applications to carbon dioxide, ozone, methane, nitrous oxide, and the
732 halocarbons," *J. of Geophys. Res.* **100**,16519-16535, (1995).

- 733 49. Delahaye, T., S. E. Maxwell, Z. D. Reed, H. Lin, J. T. Hodges, K. Sung, V. M. Devi, T. Warneke, P.
734 Spietz, and H. Tran, "Precise methane absorption measurements in the 1.64 μm spectral region for the
735 MERLIN mission." *Journal of Geophysical Research: Atmospheres* **121**.12, 7360-7370, (2016).
- 736 50. Bosilovich, Michael G., "Regional Climate and Variability of NASA MERRA and Recent
737 Reanalyses: U.S. Summertime Precipitation and Temperature", *J. Appl. Meteor.*
738 *Climatology*, **52**, 1939–1951, (2013). doi: <http://dx.doi.org/10.1175/JAMC-D-12-0291>.
- 739 51. Rienecker, M.M., Suarez, M.J., Gelaro, R.; Todling, R., Bacmeister, J., Liu, E.; Bosilovich,
740 M.G., Shubert, S.D., Takacs, L., Kim, G.-K., et al., "MERRA: NASA's modern-era
741 retrospective analysis for research and applications". *J. of Climate*, **24**, 3624–3648, (2011).
- 742 52. Li, Steven, Haris Riris, Kenji Numata, Stewart Wu, Demetrios Poullos, Anand Ramanathan,
743 James Abshire, and Michael Krainak. "Tunable narrow linewidth laser source for a methane
744 lidar," *Aerospace Conference, 2012 IEEE*, pp. 1-8. IEEE, (2012).
- 745 53. Shibata, Yasukuni, Chikao Nagasawa, and Makoto Abo. "Development of 1.6 μm DIAL
746 using an OPG/OPA transmitter for measuring atmospheric CO₂ concentration profiles."
747 *Applied Optics* **56**, no. 4, 1194-1201, (2017).
- 748 54. Kulatilaka, W. D., et al. "Development of injection-seeded, pulsed optical parametric
749 generator/oscillator systems for high-resolution spectroscopy," *Applied Physics B: Lasers*
750 *and Optics*, **80.6**, 669-680, (2005).
- 751 55. White, Kenneth O., and Stuart A. Schleusener. "Coincidence of Er: YAG laser emission with
752 methane absorption at 1645.1 nm." *Applied Physics Letters* **21.9**, 419-420, (1972).
- 753 56. Wang, X., et al. "Dual-wavelength Q-switched Er: YAG laser around 1.6 μm for methane
754 differential absorption lidar." *Laser Physics Letters* **10.11** (2013): 115804.
- 755 57. Tang, Pinghua, et al. "Stable and wavelength-locked Q-switched narrow-linewidth Er: YAG
756 laser at 1645 nm." *Optics express* **23.9**, 11037-11042, (2015).

- 757 58. Fritsche, H., O. Lux, X. Wang, Z. Zhao, and H. J. Eichler. "Resonantly diode pumped Er:
758 YAG laser systems emitting at 1645 nm for methane detection." *Laser Physics Letters* **10**, no.
759 10, 105805, (2013).
- 760 59. Gao, Chunqing, Lingni Zhu, Ran Wang, Mingwei Gao, Yan Zheng, and Lei Wang. "6.1 W
761 single frequency laser output at 1645 nm from a resonantly pumped Er: YAG nonplanar ring
762 oscillator." *Optics letters* 37, no. **11**, 1859-1861, (2012).
- 763 60. Kudryashov, Igor, and Evgenii Kotelnikov. "Tunable Q-switched Solid State Laser for
764 Methane Detection." SPIE LASE, pp. 100821I-100821I, International Society for Optics and
765 Photonics, 2017.
- 766 61. M Mackenzie, Jacob, James Grant-Jacob, Stephen Beecher, Haris Riris, Anthony Yu, David
767 Shepherd, and Robert Eason, "Er:YGG planar waveguides grown by pulsed laser deposition
768 for LIDAR applications." SPIE LASE, 100820A-100820A, International Society for Optics
769 and Photonics, 2017.
- 770

771 Figure Captions

772

773 Fig. 1. Two-way atmospheric transmittance near 1650.96 nm a from a 400 km orbit using the
774 2008 HITRAN database and a US standard atmosphere. The CH₄ line is mostly isolated
775 from adjacent CO₂ and H₂O vapor lines.

776 Fig. 2. Simplified functional block diagram of our IPDA lidar. The lidar can use one of two
777 different laser transmitters using a movable selection mirror: An Optical Parametric
778 Amplifier (OPA) or an Optical Parametric Oscillator (OPO). The transmitters use DFB
779 diode lasers for seed lasers but different pump lasers. Only one laser transmitter is operating
780 during flight.

781 Fig. 3. Example of temporal shape of the OPA burst pulse from the energy monitor detector
782 showing individual pulses within the burst pulse.

783 Fig. 4. The GSFC IPDA lidar installed on the NASA DC-8 airborne laboratory, in Palmdale,
784 CA. The transceiver structure supported two optical benches for the OPO and OPA, the
785 receiver telescope, and the transmit optics components. The overall transceiver dimensions
786 were approximately 0.9×2.0×0.8 m³ and the total weight was 363 kg. Two instruments racks
787 on either side of the transceiver contained the control and data acquisition electronics.

788 Fig. 5 Flight tracks for the 2015 flights. Flight 1 (blue), Flight 2 (red), Flight 3 (magenta).

789 Fig. 6. Flight altitude (range) in m vs. time in UTC seconds since midnight as measured by
790 the GPS receiver and our IPDA lidar for all three flights. The differences between the GPS
791 and the IPDA lidar range are due to topography. The GPS measures the altitude above the
792 mean sea level (or reference ellipsoid) but the IPDA lidar range is the altitude (range) above
793 ground, which includes the topography.

794 Fig. 7 Theoretical CH₄ transmittance from a 400 km altitude with a US standard atmosphere
795 and a comparison of the approximate wavelength sampling by the OPA (black open squares,
796 20 wavelengths) and OPO (red solid circles, 5 wavelengths). For clarity, the OPO
797 wavelengths are labeled $\lambda_1, \lambda_2, \lambda_3, \lambda_4, \lambda_5$.

798 Fig. 8. Time series data for flight 1 showing the in-situ CH₄ mixing ratio as measured by the
799 Picarro, the theoretical CH₄ mixing ratio (set at 1900 ppbv), and the CH₄ mixing ratio values
800 by our retrieval algorithm. Outliers due to instrument adjustments and clouds were filtered
801 out.

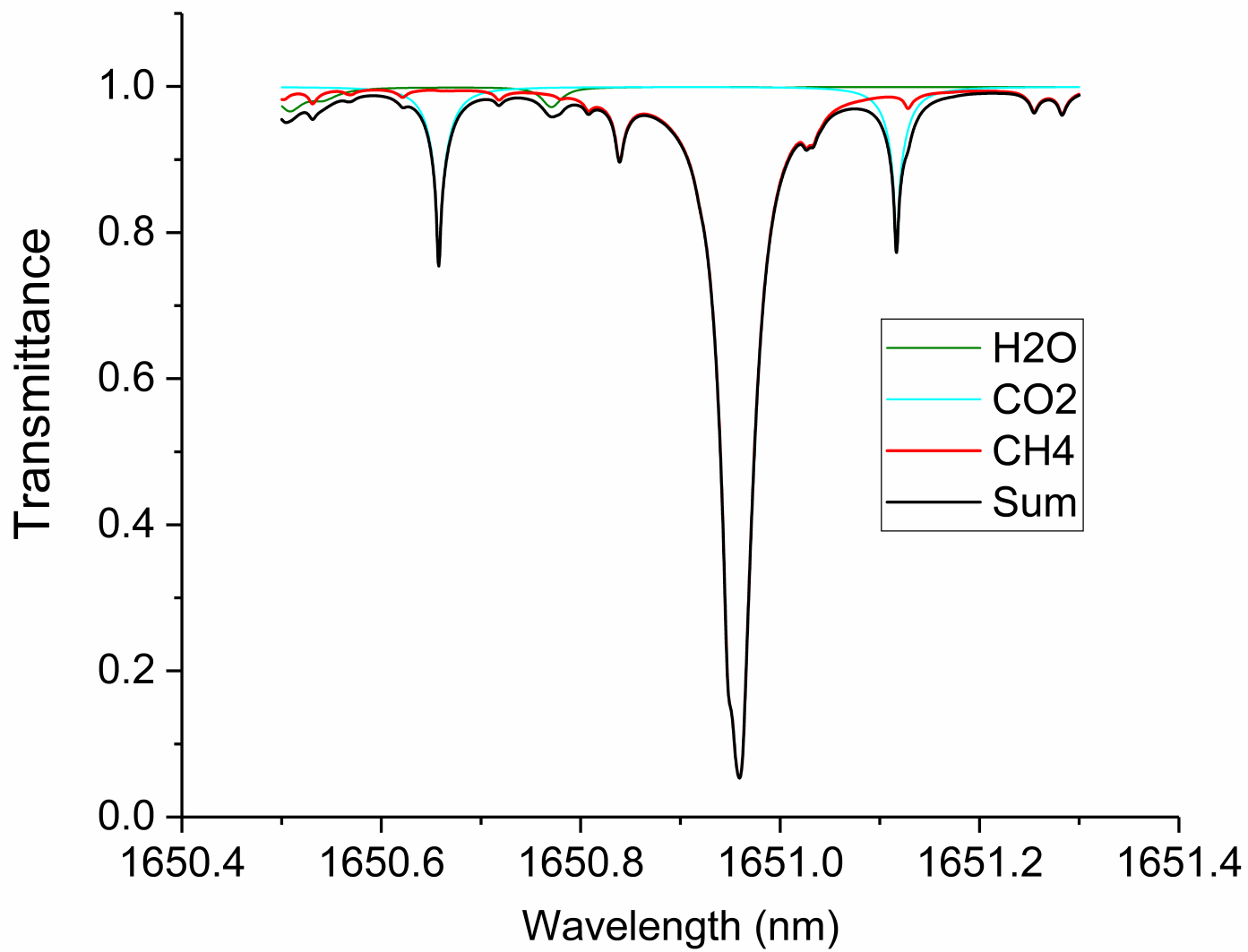
802 Fig. 9. Lidar DOD vs. Theoretical DOD for flight 1. The linear fit (without the outliers) had a
803 slope of 0.98 and an offset of -0.007 and R² value was 0.994.

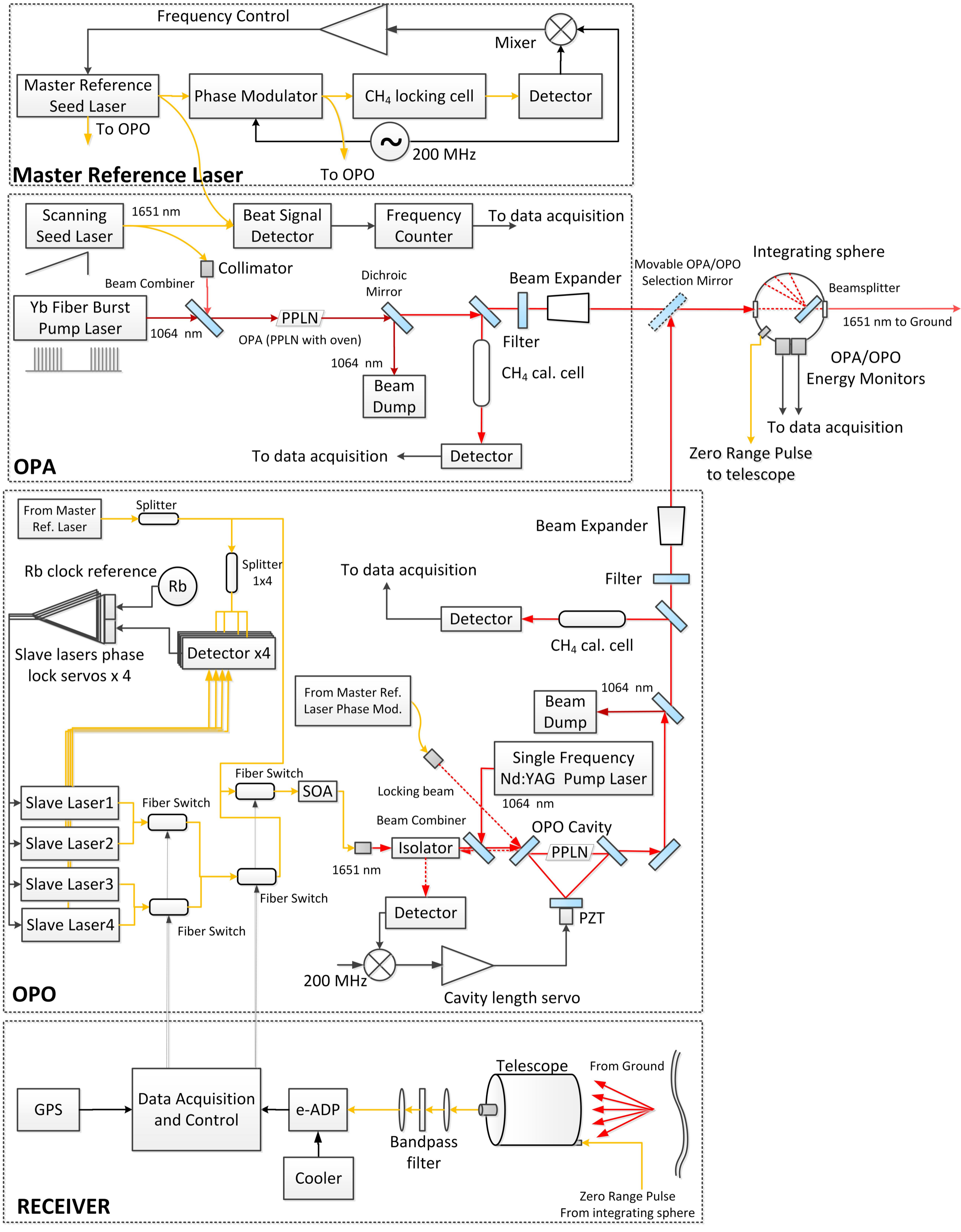
804 Fig. 10 Time series for flight 2 data showing the in-situ CH₄ mixing ratio as measured by the
805 Picarro, the theoretical CH₄ mixing ratio (set at 1900 ppbv), and the CH₄ mixing ratio values
806 by our retrieval algorithm. Outliers due to instrument adjustments and clouds were filtered
807 out.

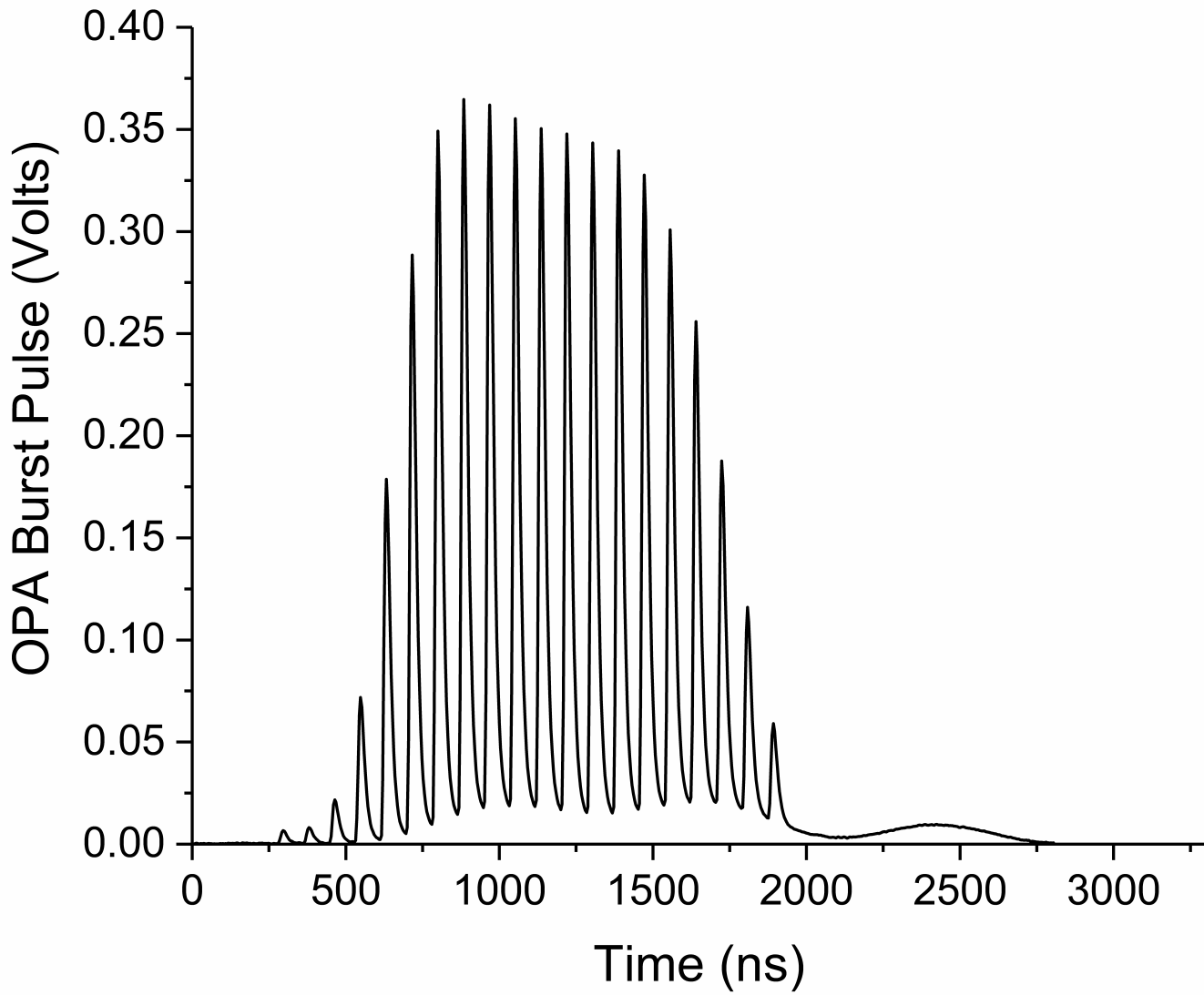
808 Fig. 11. Lidar DOD vs. Theoretical DOD for flight 2. The linear fit (without the outliers) had
809 a slope of 0.998 and an offset of -0.007 and R² value was 0.990.

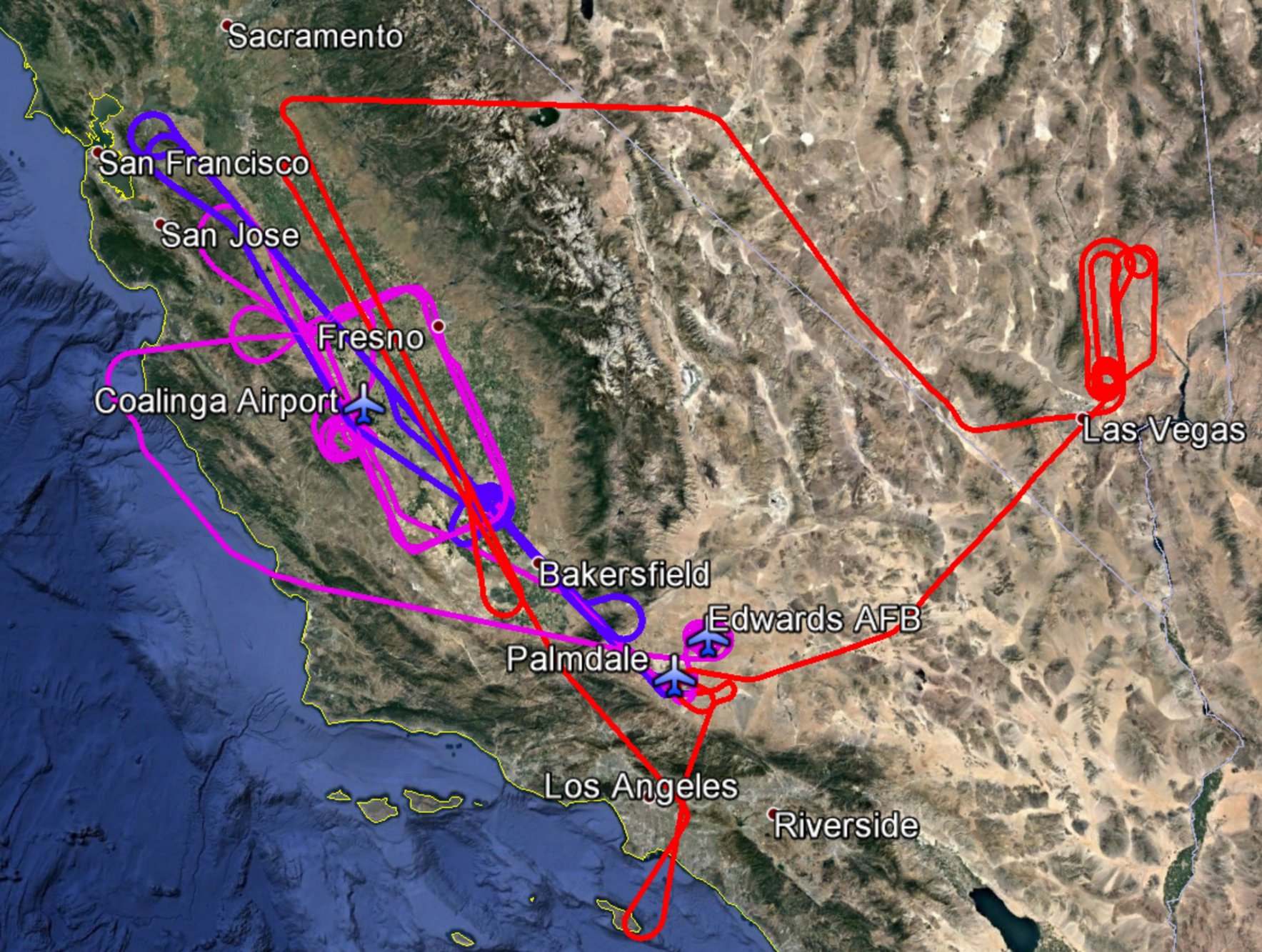
810 Fig. 12 Time series for flight 3 data showing the in-situ CH₄ mixing ratio as measured by the
811 Picarro, the theoretical CH₄ mixing ratio (set at 1900 ppbv), and the CH₄ mixing ratio values
812 by our retrieval algorithm.

813 Fig. 13. Lidar DOD vs. Theoretical DOD for flight 3. The linear fit had a slope of 1.01 and
814 an offset of -0.003. The R² value was 0.999.









Sacramento

San Francisco

San Jose

Fresno

Coalinga Airport

Bakersfield

Edwards AFB

Palmdale

Los Angeles

Riverside

Las Vegas

